MAGNETIC INDUCTION TO CROSS THE AIR-WATER INTERFACE

by

Adam Forget

Submitted in partial fulfillment of the requirements
for the degree of Master of Applied Science

at

Dalhousie University
Halifax, Nova Scotia
August 2022

© Copyright by Adam Forget, 2022

Table of Contents

List of Tables . . . . . **v**

List of Figures . . . . . **viii**

Abstract . . . . . **ix**

Acknowledgements . . . . . **x**

Chapter 1 Introduction **1**

1.1 Motivation 1

1.2 Problem Statement 2

1.3 Current State-of-the-Art 5
1.3.1 Domingo's model in water 6
1.3.2 Guo et. al complete model for both coils underwater 7
1.3.3 Gibson and Wait's approximation 8
1.3.4 Watson's finite-difference time domain simulations 9
1.3.5 Other Publications 11

1.4 Thesis Organization 11

Chapter 2 Derivation of the Mutual Inductance and Circuit Analysis **13**

2.0 Notation 13

2.1 Maxwell's Equations in Air and Water 14
2.1.1 Derivation of the Vector Potential Equation 14
2.1.2 Note on the Wavenumber k 17

2.2 Solution using Green's Function 19
2.2.1 General Form 19
2.2.2 Solution for a Coil 20

2.3 Solution using Transforms 22
2.3.1 General Procedure 22

2.4 Solution with the Air-Water Interface 28

2.5 Mutual Induction 30
2.5.1 Mutual Inductance Definition 32
2.5.2 Mutual Induction in a Single Medium 32

2.5.3 Mutual Induction with an Air-Water Interface 34
2.5.4 Induced Voltage 36
2.5.5 Comparison with Gibson's Results 38

2.6 Circuit Analysis 39
2.6.1 Transmitter Circuit Model 39
2.6.2 Receiver Circuit Model with no Capacitor 41
2.6.3 Receiver Circuit Model with a Capacitor 42
2.6.4 Repeater Circuit 43

Chapter 3 MI Link Measurements 48

3.1 Equipment 48
3.1.1 Transmitter and receiver coils 48
3.1.2 Resistors and Capacitors 50
3.1.3 Power supply, power amplifier, and signal generator in the transmitter 54
3.1.4 Receiver Amplifiers 54
3.1.5 Oscilloscope 55
3.1.6 Summary 55

3.2 Air Tests in the Lab 57
3.2.1 Test1 - Verify Mutual Inductance Formula 57
3.2.2 Test2 - Capacitor Performance 59

3.3 Air-Water Tests in the Dalhousie Aquatron 60

Chapter 4 Results and Discussion 64

4.1 Data Analysis 64

4.2 Results of Air Test 1 - Mutual Induction vs Distance 66
4.2.1 Results 67
4.2.2 Discussion 70

4.3 Results of Air Test 2 - Capacitor in the Receiver 70
4.3.1 Results 72
4.3.2 Discussion 73

4.4 Aquatron Results 74

Chapter 5 Conclusion 76

5.1 Conclusion 76

5.2 Future Work 77

Appendix A Vector Calculus Review **79**

A.1 The gradient 80

A.2 The curl 80

A.3 The divergence 81

A.4 The Laplacian 81

Bibliography **83**

List of Tables

3.1 Table of the impedance values of the TX coil labeled green. The frequency is f, the impedance is $Z = |Z| \exp(j\theta) = R + jX$, and the self-inductance is L. 51

3.2 Table of the impedance values of the TX coil labeled yellow. The frequency is f, the impedance is $Z = |Z| \exp(j\theta) = R + jX$, and the self-inductance is L. 51

3.3 Table of the impedance values of the TX coil labeled blue. The frequency is f, the impedance is $Z = |Z| \exp(j\theta) = R + jX$, and the self-inductance is L. 52

3.4 Table of the impedance values of the RX coil. The frequency is f, the impedance is $Z = |Z| \exp(j\theta) = R + jX$, and the self-inductance is L. 53

3.5 Table of the impedance values of the 15 μF capacitor used to resonate at 8 kHz. The frequency is f, the impedance is $Z = |Z| \exp(j\theta) = R + jX$, and the capacitance is C. 53

3.6 Table of the measured gains in the chain of receiver amplifiers. 56

3.7 Summary of the parameters used in the mutual inductance measurements in the air. 59

3.8 Summary of the parameters used in the voltage ratio measurements with a capacitor. 60

3.9 Summary of the parameters used in the Dalhousie Aquatron measurements. 63

4.1 Sample voltage ratio data obtained for a mutual induction system with the coils 1 m apart. 68

4.2 Table with the measured mutual inductances as a function of distance. 69

List of Figures

1.1 Model for an MI system as part of a complete underwater acoustic system. 3

1.2 Simulation results using Watson's finite-difference time domain (FDTD) model compared to Gibson and Wait. 10

2.1 Drawing of the current density **J** and its relation to **H** as described in equation (2.1). 15

2.2 Plot of the permitivity versus frequency of sea water at 14°C given by [1]. The dotted red line is the approximation $\sigma/2\pi f$ with $\sigma = 3.61$ S/m seen in equation (2.3) 16

2.3 Visual representation the relationship between **E** and **A** given by equation (2.8a). **E** and **A** are parallel. 18

2.4 Visual representation the relationship between **H** and **A** given by equation (2.6). **A** circulates around **H**. The right-hand rule gives the orientation. 18

2.5 Coil configuration 21

2.6 Contour plot, $\mathscr{C}(R)$, used to evaluate the integral in ___. $\mathscr{C}(R)$ consists of a linear path from $-R$ to R (denoted $l_{[-R,R]}$) and a counter-clockwise oriented semicircle from R back to $-R$ (denoted $\Gamma(R)$). The red curves are where the poles $\tilde{k_z} = \pm K_z = \pm\sqrt{k^2 - k_s^2}$ are located. 25

2.7 Air-water coil configuration 28

2.8 Air-water coil configuration for use in deriving the mutual inductance. 31

2.9 Plot of the reduced MI ratio function $\bar{\mathscr{M}}(\Omega)$ defined from equation (2.68a) in air with the near-field and the far-field radiation approximation. The distance between the coils is $d = 20$ m . . 34

2.10 Plot of the reduced MI ratio function $\bar{\mathscr{M}}(\Omega_w, \Omega_0, \mathscr{H})$ defined from equation (2.73a) in air with the near-field, the far-field, and the intermediate-field approximations. The TX depth is $d = 19$ m and the height $h = 1$ m. 36

2.11 Plot of the normalized induced voltage over transmitter current $\mathscr{F}$ function defined in equation (2.77) versus frequency for a fixed RX coil height of 1 meter and various TX coil depths. . . 37

2.12 Plot of Magnetic Induction in air-water from equation (2.72) and from Wait's (2.78). 38

2.13 Circuit diagram for the transmitter coil. 40

2.14 Plot showing the relationship between the amplitude of the transmitter current $|I_{TX}|$ with frequency and how it is affected by the presence of a resistor R_{TX}. 40

2.15 Circuit diagram for the receiver coil. 41

2.16 Plot showing the relationship between the amplitude of the voltage ratio $\mathscr{V}$ from equation (2.82) with frequency. 42

2.17 Circuit diagram for the receiver coil with a capacitor in parallel. 43

2.18 Air-water repeater configuration. 44

2.19 Circuit diagram for the repeater coil. 45

2.20 Contour plot (in decibels) of the ratio $\mathscr{V}_{\text{With Repeater}}/\mathscr{V}_{\text{No Repeater}}$ from equations (2.90) and (2.85) as a function of the ratio of repeater distance to antenna distance and the ratio of repeater radius to transmitter radius. 47

3.1 Image of the transmitter with the exterior open. 49

3.2 Image of the transmitter with the exterior closed. The yellow and green tapes show the coil orientations. 49

3.3 Image of the Hewitt-Packer 4192A LF Impedance Analyzer used to measure the impedances of all coils and capacitors. . . 50

3.4 Image of the Receiver. 52

3.5 Image of the APEX EVAL68 rev. B power amplifier used to boost the current in the transmitter. 54

3.6 Image of the Agilent Technologies InfiniVision DSO-X 3034A digital oscilloscope used to record the signals. The green signal comes from resistor R_{TX} and the blue signal comes from the receiver after the chain of operational amplifiers 56

3.7 Schematic of the equipment. 57

3.8 Image of the wooden cart used to perform air tests. 58
3.9 Diagram of the Aquatron test setup. 61
3.10 Photograph of the Aquatron test setup. 61
3.11 Closer look at the underwater transmitter with a weight tied onto. 62
3.12 Image of the equipment used to power the transmitter and measure the receiver. 63

4.1 Image representation of the directory structure used to store the measured voltages. 65
4.2 Sample view of a CSV file containing the measured voltages from the oscilloscope. 66
4.3 Flowchart of the process of taking the voltages measured from a CSV file to a peak-to-peak voltage. 66
4.4 Sample image of the analysis of the measured signals. A band-pass filter is used followed by a best-fit sinewave. 67
4.5 Sample plot of the voltage ratio vs frequency obtained from the mutual induction system with coils separated 1 m apart. . . . 68
4.6 Plot of the measured mutual inductance as a function of distance in the first experiment (subsection 3.2.1) along with the expected curve given by equation (3.1a). 69
4.7 Plot of the measured voltage across the receiver (with gains) at $d = 4$ m and $f = 10$ kHz along with the least-square fit to the filtered sinewave. 71
4.8 Plot of the voltage ratio in test 2 (subsection 3.2.2) with no capacitor along with the best-fit function from equation (4.1). 72
4.9 Plot of the voltage ratio in test 2 (subsection 3.2.2) with a capacitor along with the best-fit function from equation (2.85). 73
4.10 Plot of the ratio of figure 4.9 to figure 4.8. 74
4.11 Plot of the measured voltage ratio obtained from the Aquatron along with two best-fit functions and the predicted result. . . . 75

Abstract

Underwater communication from a source underwater to a destination in air is a challenging problem. Acoustic waves underwater cannot cross the interface to the air while electromagnetic waves are attenuated due to the conductivity of water. In this work, the use of magnetic induction is investigated. Specifically, to cross the air-water boundary, a detailed derivation of the magnetic induction between two coils is introduced: one underwater and the other, above the surface. This new model is compared to a simpler model given by Wait. A circuit analysis is performed on both a transmitter coil underwater and a receiver coil in the air. The ratio of the induced voltage of the receiver over transmitter current as a function of frequency is analyzed in order to find the optimal frequency at a given coil separation. The addition of a passive repeater between the coils is also investigated to determine if it improves performance. This is found to be true only when the repeater is ten times the size of the antenna coils, or when the repeater is very close.

To further verify the model a transmitter and receiver circuit is designed and constructed. Then tests are performed in the lab in air to verify that the system works. Sinusoidal signals are applied to the transmitter and are then measured at the receiver in order to measure the mutual inductance. The attenuation between the transmitter and receiver coil is compared with the theory. A similar test is deployed in the Dalhousie Aquatron. The experiments agree with the theory for distances up to 1.6 meters, after which a noise floor is reached.

Acknowledgements

I want to thank Prof. Jean-Francois Bousquet and the UWStream team for the opportunity to gain experience in underwater acoustic communication. It has been a valuable learning experience that I hope to take with me in my future endeavors. I would also like to thank Cole Ferguson for his help on designing and building the transmitter circuit used in this thesis. Thanks as well to Cole and Jeff for the few times we stepped away from responsibilities to relieve some stress and play video games.

My heartfelt thanks to my parents for their support me during my BSc, MSc, and MASc studies. Thanks to my Aunt Vicki for her support and guidance. Finally, thanks to my longtime friend Maxim for hanging out with me and always being there when I need a friend.

Chapter 1

Introduction

1.1 Motivation

Marine biologists, climatologists, and marine based industries are among the many fields that rely upon timely, reliable data gathered underwater. However, underwater communication has proven to be challenging problem. It is a very important problem to solve since these fields are vital to maintaining a healthy marine environment and are worth billions in revenue to coastal economies.

Currently, one can place a buoy on the surface to relay the underwater signal to the air. However, this approach is problematic for long term data collection due to cost and the risk of external variables which may tamper with the data. For example, climate change is increasing the frequency and severity of storm surges and tropical windstorms. Surface instruments are also vulnerable to watercraft and marine life strikes. Additionally, this approach is more costly because additional equipment, with its own power source, is required to relay the data.

Ideally, one would want to transmit data directly from underwater equipment across the air-water interface. While communication between two nodes in air or underwater is mature, sending signals between a node under the sea surface to a receiver antenna in the air remains challenging.

To date, the efforts have focused primarily on two methods to enable peer-to-peer wireless communication; acoustic and electromagnetic radiation. Electromagnetic radiation, which includes radio waves commonly used in air-to-air links, is not feasible since the conductivity of sea water decreases the radiation intensity at an exponential rate [2]. This makes electromagnetic signals impractical at distances of more than 10 meters underwater. Acoustic radiation travels very far underwater, but there are

other challenges. First, acoustic noise from ships and wind must be taken into account. Second, there is significant multipath fading, especially in narrow channels. But the greatest disadvantage is that underwater sound is not able to cross the air-water boundary [3]. Indeed, the surface acts as a perfect reflector for underwater sound waves and thus makes it impossible for use as a underwater-to-air communication tool.

There have been improvements in using acoustic waves to communicate from the water to air. [4, 5] verified the idea of using sonar to make visible ripples on the surface that can then be detected via radio frequency in the air, a process called *transnational acoustic-RF communication* or TARF. But this technology is still in its infancy and it is susceptible to noise on the surface of water.

1.2 Problem Statement

As an alternative to the above two communication methods, this thesis explores the viability of magnetic induction as a potential vehicle for data transmission. Specifically, in this proposal, two inductors are employed; an underwater transmitter, and a receiver in the air (figure 1.1). Underwater equipment is used to apply a waveform to the transmitter coil and record its output. The data is a set of sinewaves which create a changing magnetic field, and further induces a current in an air inductor.

Unlike acoustic waves, this method of communicating have the advantage of being able to cross the air-water boundary. It is less susceptible to noise, and has no multipath fading. When compared with electromagnetic signals, magnetic induction is less affected by the conductivity of sea water. The only drawback for magnetic induction is that the near-field strength of the signal is reduced by the cube of the distance. However, this would be a significant improvement over the use of electromagnetic waves which experience exponential decay.

The objective of this thesis is to develop a new mathematical model to calculate the mutual inductance between a coil underwater and another in air. The purpose is to develop a tool to assist engineers in designing underwater to air communication

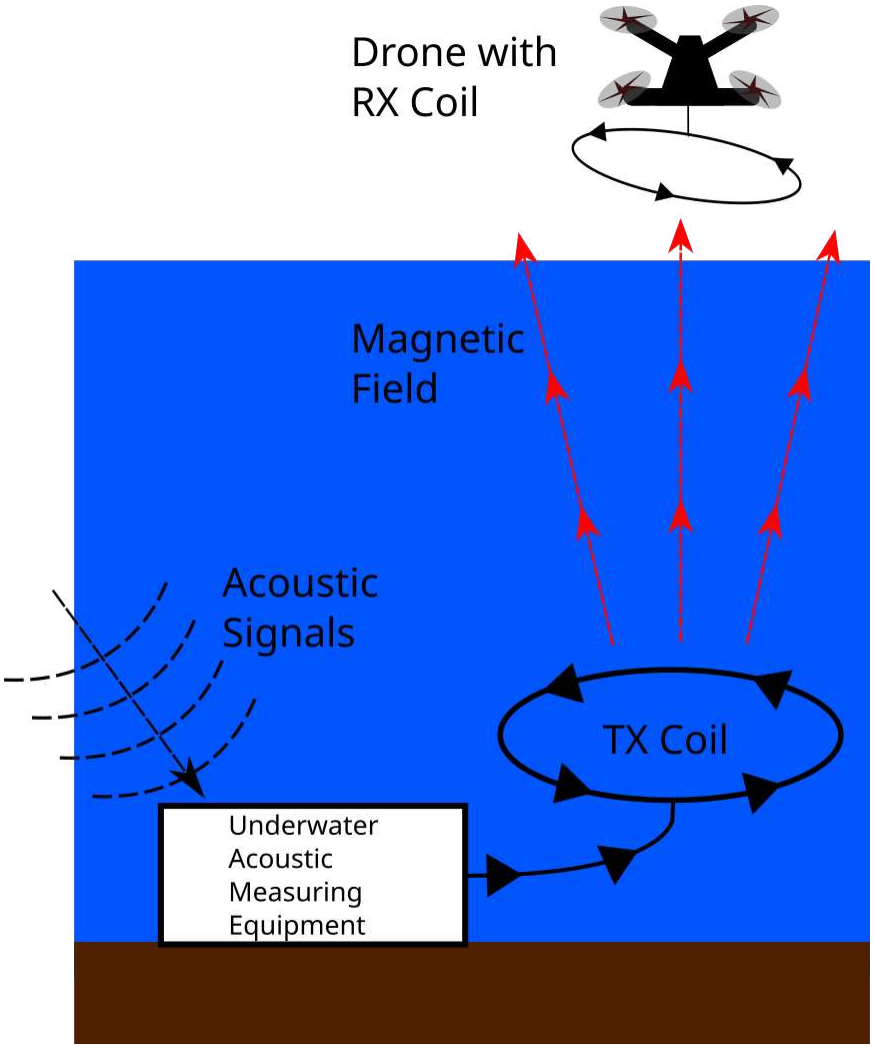

Figure 1.1: Model for an MI system as part of a complete underwater acoustic system.

systems using magnetic induction. Specifically, the goal is to develop a model that can be used to optimize the operating frequency of the MI link.

In this work, a mathematical model is developed based upon Maxwell's equations. Then a Python script is written to compare the new mathematical model with models in the literature where mutual inductance is employed in either an air-air or water-water context. A circuit is designed and built to test the proposed model. The tests are conducted in the UWStream lab in air and at the Dalhousie Aquatron in air-water, both at Dalhousie University. A second Python program is written to process the data so that test results are compared with the intended results.

In the model, circular coils with multiple turns were represented by a current density vector field with a sinusoidal current at a fixed frequency. Maxwell's equations in the frequency domain were used to derive the magnetic field from current density. The model includes a complex permitivity in Maxwell's equations, based on the conductivity of the water.

Prior to obtaining the mutual inductance in air-water, the magnetic field are found for water only. To simplify Maxwell's equations, a vector potential is introduced to reduce the four equations to one. To solve the equation, cylindrical coordinates are chosen to take advantage of the presence of azimuthal symmetry in the system. This simplifies the vector potential equation to a scalar equation. Then a series of integral transforms are used to find the scalar solution. This solution is significant because it can be used to find the magnetic field in water.

The magnetic field solution is then extended to cross the air-water interface. This is done by representing the magnetic field as a superposition of cylindrical waves. The boundary conditions in air-water are then applied to get the magnetic field in air. Mutual inductance can now be calculated by applying Faraday's law to find the flux of the magnetic field across the receiver coil.

The mutual inductance model is compared to research published by Gibson and

Wait's model [6, 7], which treated the coils as magnetic dipoles. This comparison is undertaken by the development of a Python program which plotted the mutual inductance from both models as a function of frequency for a transmitter coil at a depth of 19 meters and a receiver at a height of 1 meter.

A circuit transformer model is adopted to find the voltage ratio of an air-water coil antenna link. The proposed mutual inductance model was applied as a parameter in the circuit analysis. Plots of the ratio of the receiver voltage to transmitter current were obtained to determine the optimal frequency to resonate the system at a given coil separation.

In [2], Domingo proposed a series of passive repeater coils to increase the receiver induced voltage. In this work, the proposed model is extended to examine the value of including a repeater and identify the conditions, if any, where their use results in improved performance. This is undertaken through the development of another Python program and compared with measurements to confirm the validity.

All equipment is characterized prior to the experiments to confirm that limitations identified though the data sheets are accurate, and that all equipment are functioning within expected parameters. The proposed model is then tested experimentally both in the air and at the Dalhousie Aquatron. The results are expected to demonstrate to viability of mutual induction as a mode of water-air data transmission.

1.3 Current State-of-the-Art

Use of mutual induction for underwater communication goes back to the second world war; however one of the earliest published work on mutual induction for underwater-to-air communication was by Durrani [8], who modeled the coils as dipoles. Durrani found the magnetic field in terms of Sommerfield integrals which is consistent with more recent publications shown in this section. [9] increased popularity in the idea of underwater MI communication. However interest in mutual inductance to cross the air-water boundary started to grow significantly around 2012 when Domingo's work was published.

In this section, the most prominent work on MI is presented. Section 1.3.1 discusses Domingo's analysis of the transmission loss from mutual induction and how it compares with other communication methods. Section 1.3.2 briefly summarizes the theory by Guo et. al. if both coils are underwater. In section 1.3.3, the mutual induction from Gibson and Wait are presented. Section 1.3.4 summarizes the work by Watson on using a finite-difference time domain approach to find the induced voltage. Other publications on underwater magnetic communication are found in section 1.3.5.

1.3.1 Domingo's model in water

In [2] , Domingo studies the transmission loss of a near-field transmission model inside both fresh water and sea water consisting of two circuits with coils that can transmit power via mutual induction. The author models the system using an equivalent two-port network to determine the transmission loss between the coils as a function of the frequency of operation as well as the number of turns of the coils. The mutual inductance that Domingo uses is given by [10]:

$$M = \frac{\mu_0 \pi N_{TX} N_{RX} \alpha_{TX}^2 \alpha_{RX}^2}{2\sqrt{(\alpha_{TX}^2 + d^2)}}. \tag{1.1}$$

Here, N_{TX}, N_{RX} are the number of turns of the coils, α_{TX}, α_{RX} are the coil radii, and d is the distance between the coils. The author studies at frequencies that are small enough (less than 10 kHz) so that M can be modeled as in (1.1). Using this model for the mutual inductance, Domingo found the path loss under no conductivity, then added a factor of PL_α to account for the conductivity of water. By fixing the transmitter at a depth of 4.5 m, the receiver at a height of 1 m, and the number of turns in both coils to 1000, the author plots the path loss as a function of both frequency (from 0 to 2 kHz) and coil radius (from 0 to 2 m). The loss is greatest for smaller coils (around 50-60 dB) and for smaller frequencies. However for larger coils, the loss is frequency-independent and is approximately 10 dB.

Domingo compares these results with electromagnetic waves (EM) and acoustic waves. When transmitting EM waves with antennas at the same distances as in the

MI case, a 50-500 MHz signal has a path loss of 50-70 dB for freshwater and 1000-4000 dB for saltwater. Meanwhile the path loss for acoustic waves depends on the channel depth rather than than the conductivity. For shallow water, the loss is approximately 6-10 dB when the frequency is 1-10 kHz. In deeper water, the loss is 50 dB.

Domingo also introduces the idea of a series of passive coils between the MI antennas to act as a waveguide for the magnetic fields to decrease the transmission loss. By placing multiple coils equally spaced and all co-linear, the author finds that in freshwater at a frequency of 500 Hz and at a distance of 500 m, the path loss drops from 120 dB to 40-50 dB if the repeaters are 4.5 m apart. In seawater, the path loss improves by approximately 60 dB. However the MI is only better than acoustic communication when the distance is less than 50 m.

As an extension of Domingo's work, [11], focuses on increasing the bandwidth of an MI underwater communication system to enable better signal transmissions at 1 MHz.

1.3.2 Guo et. al complete model for both coils underwater

Guo, Sun, and Wang [12] present a complete model for the mutual inductance between two coils where both are submerged underwater. Their focus is a water-water communication system with air-water and water-floor boundaries, both of which affect the magnetic field. The authors use [13] as a reference for their formulae for the magnetic field of a coil oriented either co-planar to the surface or perpendicular to it. While Guo, Sun, and Wang do not demonstrate how they got their results, they do derive some approximations when the point at which one measures the field r is much larger than both the coil and the depth from the surface. They find that the fields are proportional to e^{jkr}/r^2. They also show how a lateral wave from the surface can propagate the magnetic field much further than the direct field from the source due to conductivity.

The authors compare their model with both a COMSOL simulation and a lab experiment where they use an aquarium to transmit power between two coils. For the

simulation, they plot the magnetic field strength vs distance from the coil at different frequencies between 10 kHz and 10 MHz, where the coil is 50 cm deep, has 5 turns with radius of 5 cm, and a current of 1 A passes through. The authors' equations and COMSOL simulation are in agreement. The fields strength decreases quickly up to 2 m at which point the decrease slows down. The field strength also gets smaller with increasing frequency.

In Guo, Sun, and Wang's lab test, two 10 cm square coils with 8 turns each are placed in an aquarium. They measure the induced voltage as a function of the separation between the coils (up to 1 m) and compare the results with both their model and with COMSOL. They find that the experimental results are misaligned from both their theoretical predictions and the COMSOL simulations by as much as 5 dB. They suggest that this is due to the limitation of an aquarium when representing infinite water. The models and COMSOL expect that the mediums are infinite, where as an aquarium is a small channel which acts as a waveguide. A proper analysis of the magnetic field in a small tank is required to verify this claim.

Guo et. al. also analyze the effect of a randomly oriented coil in the system, which is an important consideration in the real world deployment of an MI system underwater.

1.3.3 Gibson and Wait's approximation

In [6], Gibson analyzes a magnetic induction system for use in deployment in subterrain communication. Their work is relevant to this inquiry because the ground is also a conductor which can affect the strength of the magnetic field induced by two coils. The author's objective is to find an optimal frequency of operation for a two-coil magnetic induction system at a given distance, which is important in mining applications where miners must communicate to crew members on the surface. Gibson applies an equation from Wait [7], which gives the magnetic field from a coil underground in the vertical direction (i.e. perpendicular to the boundary). When

the coil is small enough to be modelled as a dipole:

$$H_{Gibson} = \frac{N_{TX} I_{TX} \alpha_{TX}^2}{2d^3} \int_0^\infty \frac{x^3 e^{-\left(x\frac{z}{d}+\sqrt{x^2+j2\pi\mu_0 h f\sigma}\right)}}{x+\sqrt{x^2+j2\pi\mu_0 h f\sigma}} J_1\left(x\frac{s}{h}\right) \mathrm{d}x \tag{1.2}$$

The radius for the coil is α_{TX} with turns N_{TX}. The transmitter is at a depth d underground. The conductivity is σ and the frequency of operation is f.

Gibson creates MATLAB simulations of the induced voltage on a receiver coil by a magnetic field given by (1.2) from a transmitter underground at a depth from 50 m to 1 km and a ground conductivity of 0.01 S/m. For 50 m, the optimal frequency is approximately 100 kHz and the voltage is approximately -30 dB. At 1 km deep, the optimal frequency is only 200 Hz and the induced voltage is approximately -160 dB.

1.3.4 Watson's finite-difference time domain simulations

Watson [14] models the air-underwater coil system by using finite-difference time domain (FDTD) simulations for the induced electric and magnetic fields. The author places the coils only 1 to 4 meters apart to reduce the extensive computational labour required to run the simulations and to operate at a short range frequencies of 5 kHz to 5 MHz. The current of the transmitter is fixed to 1 A, and the induced voltage in the receiver is evaluated and compared to Gibson and Wait's prediction. In all four different distance configurations, the simulations are in agreement with Gibson and Wait.

In order for the FDTD to yield accurate results, the size of the Yee cells have to be smaller than the wavelength of the field, which is inversely proportional to frequency. Thus the computational complexity becomes greater at larger frequencies. The author had to wait three days to simulate the communication system at the 1-10 MHz range. This is a disadvantage as the FDTD method. It's advantage is that it can analyse any waveform, not just sinewaves. The simulations can thus simplify the analysis of more arbitrary signals.

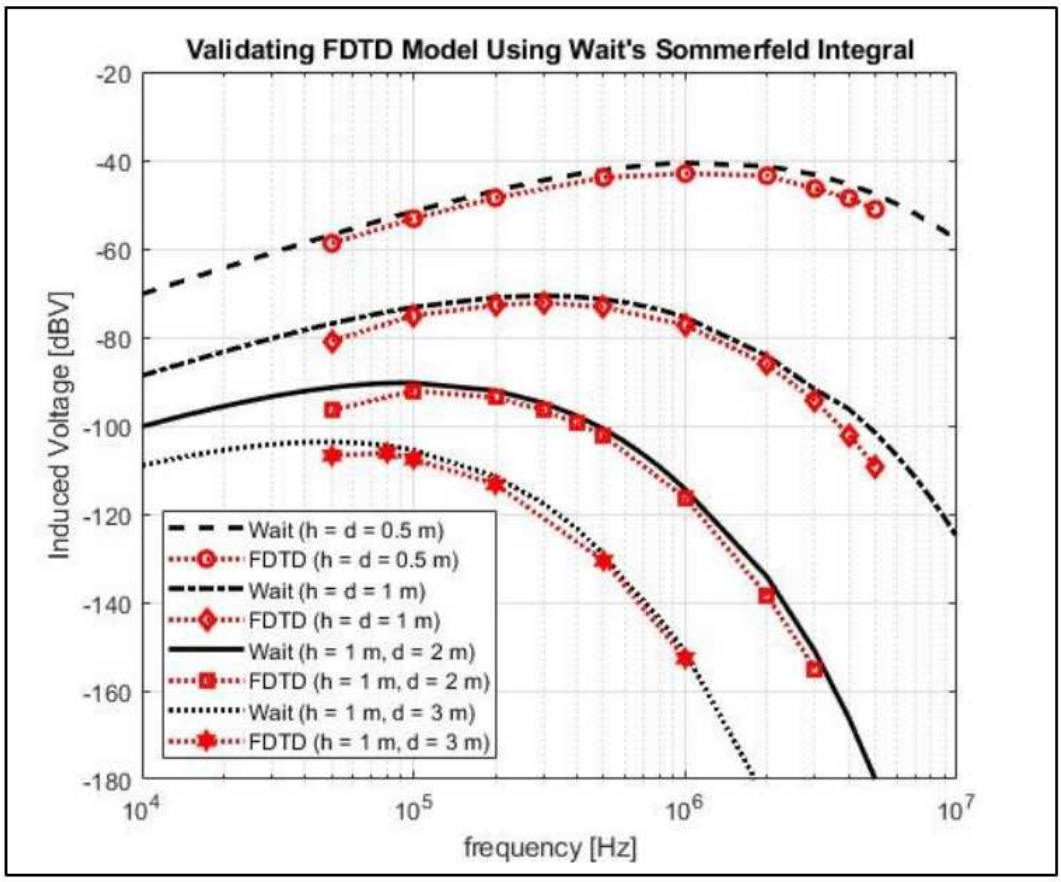

Figure 1.2: Simulation results using Watson's finite-difference time domain (FDTD) model compared to Gibson and Wait.

1.3.5 Other Publications

The reason for attenuation in a conducting medium is due to the presence of eddy currents. In [15], a methodology to analyse these eddy currents and their effect on the communication system is described. The authors modeled a conducting system with a series of coils in a non-conducting medium and developed a circuit model for the complete system. They followed up with experiments.

More recently, [16] also developed and tested an air-water MI communication system. Again, dipoles were assumed and they derived a similar result to Gibson and Wait using Hertz potentials. The authors performed an experiment where they transmitted frequency-shift keying signals.

1.4 Thesis Organization

This thesis is organized as follows. In Chapter 2, a detailed derivation of the mutual induction between a coil underwater and another in the air is obtained though the following steps. First, Maxwell's equations are simplified in terms of a vector potential. Then the potential is solved for a coil in an infinite medium. This gives rise to the fields in an infinite medium. This is followed with an extension to cross the air-water boundary using boundary conditions. Finally, the mutual induction is derived, and the end, a circuit model is developed.

In Chapter 3, an overview of the testing equipment is presented, followed by an explanation of three experiments undertaken to test the model which forms the basis of this thesis. The first is an air test in the lab to measure the mutual inductance as a function of distance. The second tests a claim in chapter 2 that a capacitor added to the receiver will improve the signal measured near a given resonance frequency. The third is conducted at the Dalhousie Aquatron to confirm that the MI air-water model works, and is in agreement with the proposed theory.

Chapter 4 begins with the methodology and a detailed data analysis. The the results of the three experiments are then presented and discussed.

Chapter 5 concludes the thesis with a summary of findings and offer suggestions for future inquiries and explorations.

Chapter 2

Derivation of the Mutual Inductance and Circuit Analysis

In this chapter, the mathematical models for the electromagnetic fields by a coil carrying a sinusoidal current at a given frequency are derived for the cases of air, water, and air-water. Then these fields are used to obtain a complete frequency-dependent formula for the mutual inductance. The formula is applied to a circuit system.

Section 2.0 presents a brief summary of the notation used in this chapter; then, in section 2.1, Maxwell's Equations in Air and Water are summarized and used to derive a vector potential which is easier to use to solve for the fields. Two methods to solve the vector potential are given in sections 2.2 (Green's function) and 2.3 (Transforms), the latter being a new method. In section 2.4 the magnetic fields are extended to cross the air-water interface. The mutual induction in three scenarios are found and presented in section 2.5 along with suitable approximations. Finally, in section 2.6, a detailed analysis of the circuits associated to the coils are presented and how the mutual inductance affects the circuits is discussed.

2.0 Notation

In the rest of this work, the following notation is adopted:

- (x, y, z) are used to denote Cartesian coordinates,
- (s, ϕ, z) are used for cylindrical coordinates ($s^2 = x^2 + y^2$, $\tan\phi = y/x$), and
- (r, ϕ, θ) are used for spherical coordinates ($r^2 = x^2 + y^2 + z^2$, $\tan\theta = s/z$).
- The vector $\mathbf{r} = x\hat{\mathbf{x}} + y\hat{\mathbf{y}} + z\hat{\mathbf{z}}$ represents a point relative to a given origin where we want to calculate a field.
- Unit vectors $\hat{\mathbf{x}}, \hat{\mathbf{y}}, \hat{\mathbf{z}}, \hat{\mathbf{s}}, \hat{\phi}, \hat{\mathbf{r}}, \hat{\theta}$ are oriented in the direction of increasing value of the coordinate of the same letter.

- The differential operator ∇ is used to denote the divergence $div(\mathbf{V}) = \nabla \bullet \mathbf{V}$, the curl $curl(\mathbf{V}) = \nabla \times \mathbf{V}$, and the Laplacian $lapl(\mathbf{V}) = \nabla^2\mathbf{V}$. Their meanings are given in Appendix A.

The electric and magnetic fields used in this text are $\mathbf{E}$ and $\mathbf{H}$ respectively, instead of $\mathbf{E}$ and $\mathbf{B}$ since that is the standard in Electrical Engineering. Note that for a general medium $\mathbf{B} = \mu_0(\mathbf{H}+\mathbf{M})$, where $\mathbf{M}$ is a magnetization field that is induced by current sources. Since this text only considers air and water, which are not magnetic mediums, $\mathbf{M} = 0$ and thus $\mathbf{B} = \mu_0\mathbf{H}$.

Recall that $\epsilon_0 = 8.85 \times 10^{-12}$ A^2 s^4/kg m^3 is the permittivity of free space, also $\mu_0 = 4\pi \times 10^{-7}$ kg m/A^2 s^2 is the permeability of free space, and $c = 1/\sqrt{\epsilon_0\mu_0} = 3.00 \times 10^8$ m/s is the speed of light in free-space.

2.1 Maxwell's Equations in Air and Water

In this section the Maxwell equations are used to derive a simpler equation, in terms of a vector potential $\mathbf{A}$, that will give the electric and magnetic fields for an arbitrary current source. This simpler equation will be solved for a coil in the next section. Section 2.1.1 goes over this derivation and section 2.1.2 makes a comment on the wavenumber which is a new quantity that appears once the equation for $\mathbf{A}$ is found.

2.1.1 Derivation of the Vector Potential Equation

In this section, the vector potential $\mathbf{A}$ is defined and derived. For this purpose, Maxwell's equations describing the relationship between the fields $\mathbf{E}$, $\mathbf{H}$ and the sources ρ, $\mathbf{J}$ will be utilized

The time dependant Maxwell's equations in any non-magnetic medium are given

as [17]:

$$\nabla \bullet \mathbf{D}(\mathbf{r}, t) = \rho(\mathbf{r}, t) \tag{2.1a}$$

$$\nabla \times \mathbf{E}(\mathbf{r}, t) = -\mu_0 \frac{\partial \mathbf{H}}{\partial t}(\mathbf{r}, t) \tag{2.1b}$$

$$\nabla \bullet \mathbf{H}(\mathbf{r}, t) = 0 \tag{2.1c}$$

$$\nabla \times \mathbf{H}(\mathbf{r}, t) = \mathbf{J}(\mathbf{r}, t) + \frac{\partial \mathbf{D}}{\partial t}(\mathbf{r}, t) \tag{2.1d}$$

See Appendix A for a review on the meaning of divergence and curl. Here, $\rho(\mathbf{r}, t)$ is the electric charge density and $\mathbf{J}(\mathbf{r}, t)$ is the current density. The relationship between $\mathbf{H}$ and $\mathbf{J}$ is illustrated in figure 2.1. $\mathbf{D}(\mathbf{r}, t)$ is a vector field, often called the electric displacement field, that depends on $\mathbf{E}(\mathbf{r}, t)$. The relationship between $\mathbf{D}$ and $\mathbf{E}$ depends on the nature of the medium. In the case of air, the relationship is simply $\mathbf{D}(\mathbf{r}, t) = \epsilon_0 \mathbf{E}(\mathbf{r}, t)$. In a *frequency-dependent and isotropic linear media*, the relationship in the frequency domain is

$$\mathbf{D}(\mathbf{r}, f) = \epsilon(f)\ \mathbf{E}(\mathbf{r}, f) \tag{2.2}$$

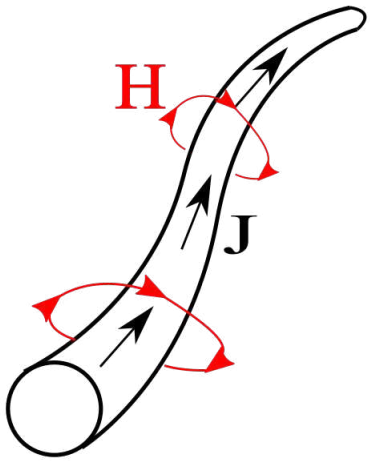

Figure 2.1: Drawing of the current density $\mathbf{J}$ and its relation to $\mathbf{H}$ as described in equation (2.1).

where $\epsilon(f)$ is the permittivity of the medium. This occurs when the induced electric field in the medium depend on the frequency of the source and is independent on

location. In air, $\epsilon(f) = \epsilon_0$ and in water (provided f is no larger than 6 GHz according to [1], see Figure 2.2), $\epsilon(f)$ is given by:

$$\epsilon_{\text{water}}(f) = \epsilon_{\text{w}} + j\frac{\sigma}{2\pi f} \tag{2.3}$$

For water, $\epsilon_{\text{w}} = 81\epsilon_0$ and $\sigma = 4$ S. In this work, it is assumed that the medium is either air, water, or both separated by a boundary.

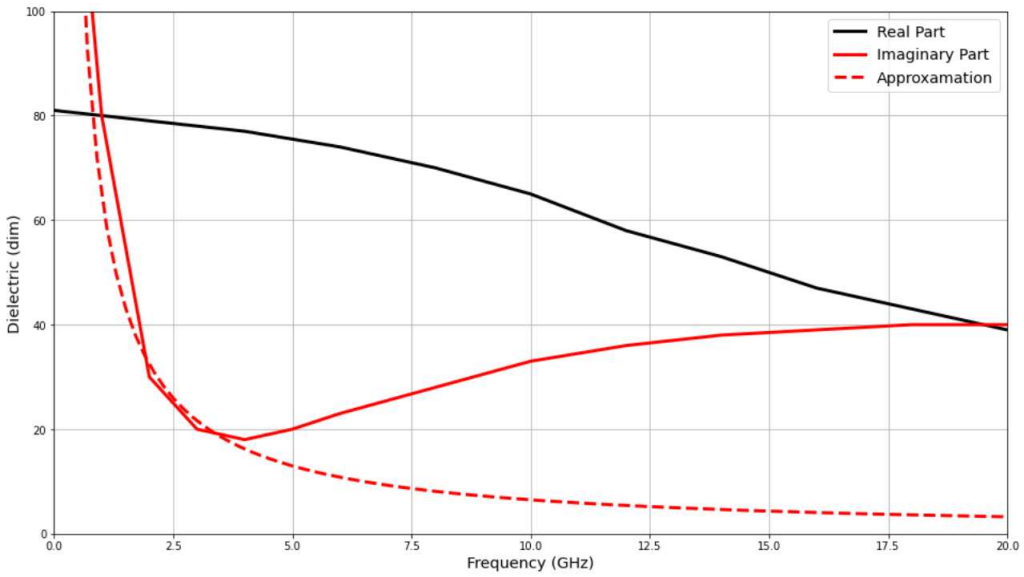

Figure 2.2: Plot of the permitivity versus frequency of sea water at 14°C given by [1]. The dotted red line is the approximation $\sigma/2\pi f$ with $\sigma = 3.61$ S/m seen in equation (2.3)

In a frequency-dependent and isotropic media (like air and water), it is best to express Maxwell's equations (2.1) in the frequency domain. This can be done using the Fourier transform. Specifically, the frequency dependent magnetic field can be obtained from $\mathbf{H}(\mathbf{r}, t)$:

$$\mathbf{H}(\mathbf{r}, t) = \int_{\infty}^{\infty} \mathbf{H}(\mathbf{r}, f) e^{j2\pi f t} \mathrm{d}f. \tag{2.4}$$

The $\mathbf{E}$, $\mathbf{D}$, ρ, and $\mathbf{J}$ are also obtained using the Fourier transfom. Also, in this work it is assumed that there are no free charges (i.e. $\rho = 0$) since the sources that are used are coils which are current sources only. Note that due to the continuity

equation of charge ($\nabla \bullet \mathbf{J} = -\frac{\partial \rho}{\partial t}$), this means that the current density must have a divergence of zero. Thus (2.1)) and ((2.2)) reduce to:

$$\nabla \bullet \mathbf{E}(\mathbf{r}, f) = 0 \tag{2.5a}$$

$$\nabla \times \mathbf{E}(\mathbf{r}.f) = -j2\pi f \mu_0 \mathbf{H}(\mathbf{r}, f) \tag{2.5b}$$

$$\nabla \bullet \mathbf{H}(\mathbf{r}, f) = 0 \tag{2.5c}$$

$$\nabla \times \mathbf{H}(\mathbf{r}, f) = \mathbf{J}(\mathbf{r}, f) + j2\pi f \epsilon(f)\ \mathbf{E}(\mathbf{r}, f) \tag{2.5d}$$

In this text, from now onwards, the functional dependence of $\mathbf{r}$ and f will be assumed and will no longer be specified). To solve (2.5), the *vector potential*, $\mathbf{A} = \mathbf{A}(\mathbf{r}, f)$, is introduced via the following two relations:

$$\nabla \times \mathbf{A} = \mu_0 \mathbf{H} \tag{2.6}$$

$$\nabla \bullet \mathbf{A} = 0 \tag{2.7}$$

As derived in [17], Eqs.(2.6) and (2.7) satisfy Eq.((2.5)) provided the following two conditions are true and the charge density is zero:

$$\mathbf{E} = -j2\pi f \mathbf{A} \tag{2.8a}$$

$$\nabla^2 \mathbf{A} + k^2 \mathbf{A} = -\mu_0 \mathbf{J} \tag{2.8b}$$

Here, $k^2 = 4\pi^2 f^2 \mu_0 \epsilon$ is the *wavenumber* which depends on both the frequency and the medium. A visual representation of these equations are given in figures 2.3 and 2.4. Equation (2.8b) is used to get the vector potential $\mathbf{A}$, given a current density vector $\mathbf{J}$. Then (2.6) and (2.8a) are used to find $\mathbf{H}$ and $\mathbf{E}$ from $\mathbf{A}$.

The vector potential are solved using two methods. In Section 2.2, equation (2.8b) are solved using the Green's function, whereas, in Section 2.3 equation (2.8b) are solved by decomposing $\mathbf{A}$ as a superposition of waves.

2.1.2 Note on the Wavenumber k

In air, the wavenumber k is simply:

$$k_{\mathrm{a}} = \frac{2\pi f}{c}, \tag{2.9}$$

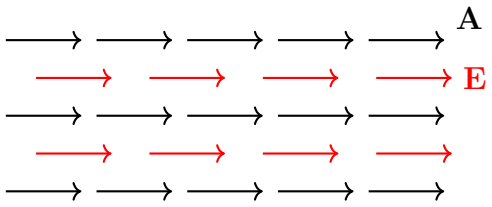

Figure 2.3: Visual representation the relationship between **E** and **A** given by equation (2.8a). **E** and **A** are parallel.

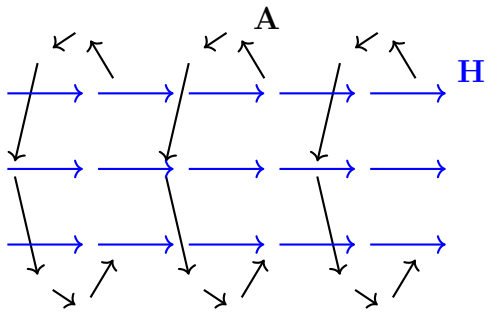

Figure 2.4: Visual representation the relationship between **H** and **A** given by equation (2.6). **A** circulates around **H**. The right-hand rule gives the orientation.

where c is the speed of light. However in water, the wavenumber is a complex number. Using $k^2 = 4\pi^2 f^2 \mu_0 \epsilon$ and ϵ from equation (2.3), one obtains:

$$k_{\mathrm{w}} = \mathscr{K}_{\mathrm{w}} + j\kappa_{\mathrm{w}} \tag{2.10a}$$

$$\mathscr{K}_{\mathrm{w}} = \frac{9\sqrt{2}\pi f}{c} \sqrt{\sqrt{1 + \left(\frac{\sigma}{162\pi\epsilon_0 f}\right)^2} + 1} \tag{2.10b}$$

$$\kappa_{\mathrm{w}} = \frac{9\sqrt{2}\pi f}{c} \sqrt{\sqrt{1 + \left(\frac{\sigma}{162\pi\epsilon_0 f}\right)^2} - 1} \tag{2.10c}$$

In (2.10), $\mathscr{K}_{\mathrm{w}}$ determines the wavelength of $2\pi/\mathscr{K}_{\mathrm{w}}$ and effectively the speed of $2\pi f/\mathscr{K}_{\mathrm{w}}$. Meanwhile, κ_{w} is a measure of the attenuation. By definition, the *skin depth*, $1/\kappa_{\mathrm{w}}$, determines when a wave travelling in the water has its amplitude reduced by a factor of $1/e$.

Since the frequencies used are less than 1 GHz, in salt water $\sigma \gg \epsilon_{\mathrm{w}} 2\pi f$, the

wavenumber can be approximated as:

$$\mathscr{K}_{\mathrm{w}} \approx \kappa_{\mathrm{w}} \approx \sqrt{\pi f \sigma \mu_0} \tag{2.11}$$

Thus the far-field (i.e. $\mathscr{K}_{\mathrm{w}} r \gg 1$), which is where radiation occurs, and the attenuation regime (i.e. $\kappa_{\mathrm{w}} r \gg 1$), which means the signal decays exponentially, always apply.

2.2 Solution using Green's Function

In this section, the magnetic field of a coil in both air and water is solved using Green's function. This method is found in elementary texts in electrodynamics [17, 18]. The advantage of this method is that the solution has an intuitive interpretation and is easier to simplify in extreme distances relative to the wavenumber. However this solution is not ideal when a boundary is introduced.

2.2.1 General Form

Equation (2.8b) can be decomposed into three equations in terms of the Cartesian components:

$$\nabla^2 A_x + k^2 A_x = -\mu_0 J_x \tag{2.12a}$$

$$\nabla^2 A_y + k^2 A_y = -\mu_0 J_y \tag{2.12b}$$

$$\nabla^2 A_z + k^2 A_z = -\mu_0 J_z \tag{2.12c}$$

Here, the solution for the x-component is demonstrated. Similar procedure can be used for the other two components.

First, the current density can be represented as a 3-dimensional point source as:

$$J_x(\mathbf{r}) = \int_{\text{All Space}} J_x(\mathbf{r}')\delta^3(\mathbf{r} - \mathbf{r}')\mathrm{d}^3\mathbf{r}' \tag{2.13}$$

Then, *Green's function*, $G_x(\mathbf{r} - \mathbf{r}')$, can be expressed as:

$$A_x(\mathbf{r}) = \int_{\text{All Space}} J_x(\mathbf{r}')G_x(\mathbf{r} - \mathbf{r}')\mathrm{d}^3\mathbf{r}' \tag{2.14}$$

Substitute (2.13) and (2.14) into (2.12a) to get:

$$\nabla^2 G_x(\mathbf{r}-\mathbf{r}') + k^2 G_x(\mathbf{r}-\mathbf{r}') = -\mu_0 \delta^3(\mathbf{r}-\mathbf{r}') \tag{2.15}$$

The structure of this equation does not change if $\mathbf{r}-\mathbf{r}'$ is replaced by $\mathbf{r}$, such that:

$$\nabla^2 G_x(\mathbf{r}) + k^2 G_x(\mathbf{r}) = -\mu_0 \delta^3(\mathbf{r}) \tag{2.16}$$

To solve (2.16), note that when $\mathbf{r} \neq 0$, the right-hand side is zero. The solution in this case is of the form:

$$G_x(\mathbf{r}) = C\frac{e^{jkr}}{r} + D\frac{e^{-jkr}}{r}, \quad r = ||\mathbf{r}|| > 0 \tag{2.17}$$

where C and D are constants that are to be determined. Note that the first term is an outwards moving wave from the origin that decays to zero at infinity (when accounting for the possible complex form of k) whereas the second term grows to infinity at increasing distances from the origin. Thus on physical grounds, it is required that $D = 0$. To find C, substitute (2.17) back into (2.16) and evaluate a volume integral over a sphere of a radius of any size to find that $C = \mu_0/4\pi$. Therefore:

$$G_x(\mathbf{r}) = \frac{\mu_0}{4\pi}\frac{e^{jkr}}{r} \tag{2.18}$$

Substitute this into (2.14) to get:

$$A_x(\mathbf{r}) = \frac{\mu_0}{4\pi}\int_{\text{All Space}} J_x(\mathbf{r}')\frac{e^{jk||\mathbf{r}-\mathbf{r}'||}}{||\mathbf{r}-\mathbf{r}'||}\mathrm{d}^3\mathbf{r}' \tag{2.19}$$

Similar equations exist for A_y and A_z. Recombining the three solution to get the vector form:

$$\mathbf{A}(\mathbf{r}) = \frac{\mu_0}{4\pi}\int_{\text{All Space}} \mathbf{J}(\mathbf{r}')\frac{e^{jk||\mathbf{r}-\mathbf{r}'||}}{||\mathbf{r}-\mathbf{r}'||}\mathrm{d}^3\mathbf{r}' \tag{2.20}$$

This last expression shows how to calculate $\mathbf{A}$ if one knows the value of $\mathbf{J}$ everywhere in space.

2.2.2 Solution for a Coil

As shown in Figure 2.5, the current density of a N-turn coil centered at the origin, parallel to the xy plane, and of radius α, provided the thickness of the coil is much smaller than the radius, is:

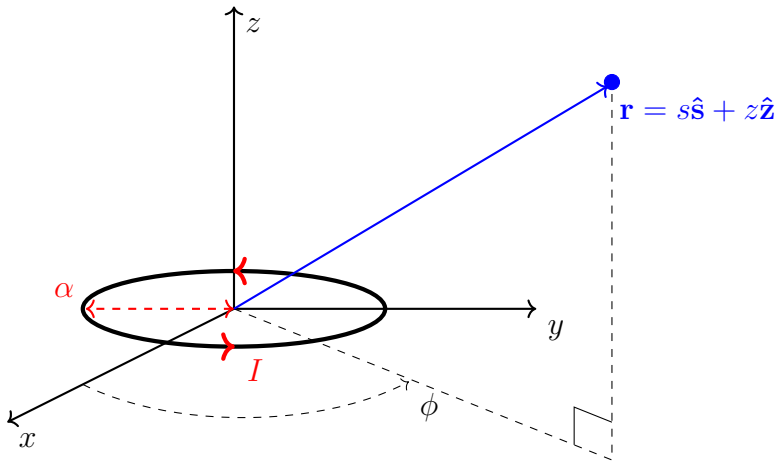

Figure 2.5: Coil configuration

$$\mathbf{J}(s,\phi,z) = NI\delta(s-\alpha)\delta(z)\hat{\phi} \tag{2.21}$$

where I is the current. In Cartesian coordinates:

$$J_x = -NI\delta(s-\alpha)\delta(z)\sin\phi \tag{2.22a}$$

$$J_y = NI\delta(s-\alpha)\delta(z)\cos\phi \tag{2.22b}$$

$$J_z = 0 \tag{2.22c}$$

Note that $A_z = 0$. Also by symmetry, $\mathbf{A}(r,\phi,\theta) = \mathbf{A}(r,0,\theta)$ Substitute (2.22) into (2.20) and, after some simplifications:

$$\mathbf{A}(r,\theta) = \frac{\mu_0 NI\alpha^2}{4\pi}\hat{\phi}\int_0^{2\pi} \frac{\cos\phi' e^{jk\sqrt{r^2+\alpha^2-2r\alpha\cos\phi'\sin\theta}}}{\sqrt{r^2+\alpha^2-2r\alpha\cos\phi'\sin\theta}}\mathrm{d}\phi' \tag{2.23}$$

This equation can be further simplified if the condition $r \gg \alpha$ is assumed. Then using Taylor expansion in α/r:

$$[r^2+\alpha^2-2r\alpha\cos\phi'\sin\theta]^{-1/2} = \frac{1}{r}\left[1+\frac{\alpha}{r}\cos\phi'\sin\theta + O\left(\frac{\alpha^2}{r^2}\right)\right] \tag{2.24}$$

$$e^{jk\sqrt{r^2+\alpha^2-2r\alpha\cos\phi'\sin\theta}} = e^{jkr}\left[1-jk\alpha\cos\phi'\sin\theta + O\left(\frac{\alpha}{r}\right)\right] \tag{2.25}$$

(2.23) simplifies to:

$$\mathbf{A} = \frac{\mu_0 N I \alpha \sin\theta}{4r} e^{jkr} \left(\frac{\alpha}{r} - jk\alpha \right) \hat{\phi} \tag{2.26}$$

The distinction between the near-field and far-field is more apparent with (2.26). In the near-field ($kr \ll 1$):

$$\mathbf{A} = \frac{\mu_0 N I \alpha^2 \sin\theta}{4r^2} \hat{\phi} \tag{2.27}$$

This is the same vector potential from a static magnetic dipole. There is no frequency dependence nor any attenuation. The vector potential is inversely proportional to the square of the distance, r, from the coil. In the far-field ($kr \gg 1$):

$$\mathbf{A} = -j \frac{k\mu_0 N I \alpha^2 \sin\theta}{4r} e^{jkr} \hat{\phi} \tag{2.28}$$

Here, $||\mathbf{A}||$ is now proportional to f. In air, $||\mathbf{A}||$ falls off by $1/r$. However in water, there is exponential drop-off with distance ($e^{-\kappa_w r}/r$).

2.3 Solution using Transforms

An alternative solution using transforms is presented here in detail. Here, the use of Fourier and Hankel transforms are used to find the vector potential in (2.8b). This results in a more complex expression for the vector potential, but this version is needed when the air-water boundary is introduced. This is a new technique developed for this thesis and is derived with the aid of [13].

2.3.1 General Procedure

It is known from (2.23) that $\mathbf{A}$ has only a ϕ-component and has asymutal symmetry, i.e. $\mathbf{A}(s, \phi, z) = A(s, z)\hat{\phi}(\phi)$. If (2.8b) is decomposed in cylindrical components instead of Cartesian, one can ignore both the A_s and A_z equations. Also set all partial derivatives with respect to ϕ to be zero. The result will be (see equation A.12):

$$\frac{\partial^2 A}{\partial s^2} + \frac{1}{s}\frac{\partial A}{\partial s} - \frac{1}{s^2} A + \frac{\partial^2 A}{\partial z^2} + k^2 A = -\mu_0 N I \delta(s - \alpha)\delta(z) \tag{2.29}$$

(Here, $J_\phi = NINI\delta(s - \alpha)\delta(z)$ as stated in (2.21))

First, the *order-1 Hankel transform* in the s-coordinate is evaluated. The order-1 Hankel transform is defined by:

$$\bar{A}(k_s, z) = \mathcal{H}_1 [A] = \int_0^\infty A(s, z) J_1(k_s s) s \, \mathrm{d}s \tag{2.30}$$

The corresponding inverse transform is:

$$A(s, z) = \mathcal{H}_1^{-1} \left[\bar{A}\right] = \int_0^\infty \bar{A}(k_s, z) J_1(k_s s) k_s \, \mathrm{d}k_s \tag{2.31}$$

One can show that:

$$\mathcal{H}_1 \left[\frac{\partial^2 A}{\partial s^2} + \frac{1}{s}\frac{\partial A}{\partial s} - \frac{1}{s^2} A\right] = -k_s^2 \bar{A} \tag{2.32a}$$

$$\mathcal{H}_1 \left[\frac{\partial^2 A}{\partial z^2}\right] = \frac{\partial^2 \bar{A}}{\partial z^2} \tag{2.32b}$$

$$\mathcal{H}_1 [\delta(s - \alpha)] = \alpha J_1(k_s \alpha) \tag{2.32c}$$

After applying the order-1 Hankel transform on (2.29), one obtains a new equation in terms of $\bar{A}(k_s, z)$ with only derivatives in z:

$$-k_s^2 \bar{A} + \frac{\partial^2 \bar{A}}{\partial z^2} + k^2 \bar{A} = -\mu_0 \alpha N I J_1(k_s \alpha) \delta(z) \tag{2.33}$$

Now a Fourier transform in the z-coordinate is applied in order to eliminate the other partial derivative:

$$\mathcal{A}(k_s, k_z) = \mathcal{F} \left[\bar{A}\right] = \int_{-\infty}^\infty \bar{A}(k_s, z) e^{-jk_z z} \, \mathrm{d}z \tag{2.34a}$$

$$\bar{A}(k_s, z) = \mathcal{F}^{-1} [\mathcal{A}] = \frac{1}{2\pi} \int_{-\infty}^\infty \mathcal{A}(k_s, k_z) e^{jk_z z} \, \mathrm{d}k_z \tag{2.34b}$$

Note that:

$$\mathcal{F} \left[\frac{\partial^2 \bar{a}}{\partial z^2}\right] = -k_z^2 \mathcal{A} \tag{2.35a}$$

$$\mathcal{F} [\delta(z)] = 1 \tag{2.35b}$$

Equation (2.33) now becomes after a Fourier transform:

$$-k_s^2 \mathcal{A} - k_z^2 \mathcal{A} + k^2 \mathcal{A} = -\mu_0 \alpha N I J_1(k_s \alpha) \tag{2.36}$$

Or more simply:

$$\mathcal{A}(k_s, k_z) = \frac{\mu_0 \alpha N I J_1(k_s \alpha)}{k_s^2 + k_z^2 - k^2} \tag{2.37}$$

Now inverse transforms are taken to get back $A(s,z)$:

$$\begin{aligned}\bar{A}(k_s,z) &= \mathcal{F}^{-1}\left[\mathcal{A}\right] \\ &= \frac{1}{2\pi}\int_{-\infty}^{\infty}\mathcal{A}(k_s,k_z)e^{jk_zz}\,\mathrm{d}k_z \\ &= \frac{\mu_0\alpha NIJ_1(k_s\alpha)}{2\pi}\int_{-\infty}^{\infty}\frac{e^{jk_zz}\,\mathrm{d}k_z}{k_s^2+k_z^2-k^2}\end{aligned} \tag{2.38}$$

It should be noted that for the integral in (2.38), the poles $k_z = \pm K_z$ (where $K_z \equiv \sqrt{k^2-k_s^2}$) can be real numbers if k is real (i.e. no conductivity like in air). This makes the integral undefined. To avoid this problem, it will be assumed that k is always complex and then, if necessary, let $\mathrm{Im}(k)\to 0$ after the integration is complete.

The integral in (2.38) can be evaluated by extending the variable of integration k_z to be a complex number $\tilde{k_z} = k_z + k_z'$ and interpreting (2.38) as a contour integral. The following contours are defined:

$$l_{[-R,R]} = \{k_z|\ -R \le k_z \le R\}, \qquad \text{Line along the real axis from } -R \text{ to } R. \tag{2.39a}$$

$$\Gamma(R) = \{Re^{jt}|\ 0 \le t \le \pi\}, \qquad \text{Semicircular arc centerd at the origin with radius } R. \text{ Oriented counter-clockwise} \tag{2.39b}$$

$$\mathscr{C}(R) = l_{[-R,R]} + \Gamma(R), \qquad \text{Total closed contour} \tag{2.39c}$$

Figure 2.6 shows a plot of the contours that will be used to solve the integral in (2.38).

Rewrite the integral in (2.38) as:

$$\begin{aligned}\int_{-\infty}^{\infty}\frac{e^{jk_zz}\,\mathrm{d}k_z}{k_z^2-K_z^2} &= \lim_{R\to\infty}\int_{-R}^{R}\frac{e^{jk_zz}\,\mathrm{d}k_z}{k_z^2-K_z^2} \\ &= \lim_{R\to\infty}\int_{l_{[-R,R]}}\frac{e^{j\tilde{k_z}z}\,\mathrm{d}\tilde{k_z}}{\tilde{k_z}^2-K_z^2} \\ &= \lim_{R\to\infty}\left(\oint_{\mathscr{C}(R)}\frac{e^{j\tilde{k_z}z}\,\mathrm{d}\tilde{k_z}}{\tilde{k_z}^2-K_z^2} - \int_{\Gamma(R)}\frac{e^{j\tilde{k_z}z}\,\mathrm{d}\tilde{k_z}}{\tilde{k_z}^2-K_z^2}\right) \\ &= \lim_{R\to\infty}\oint_{\mathscr{C}(R)}\frac{e^{j\tilde{k_z}z}\,\mathrm{d}\tilde{k_z}}{\tilde{k_z}^2-K_z^2} - \lim_{R\to\infty}\int_{\Gamma(R)}\frac{e^{j\tilde{k_z}z}\,\mathrm{d}\tilde{k_z}}{\tilde{k_z}^2-K_z^2}\end{aligned} \tag{2.40}$$

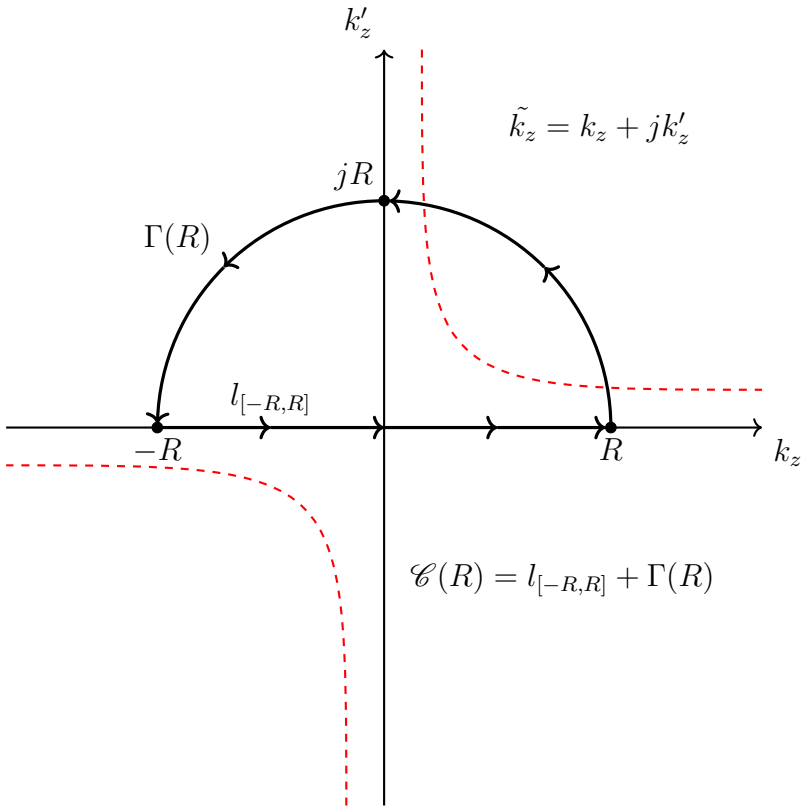

Figure 2.6: Contour plot, $\mathscr{C}(R)$, used to evaluate the integral in ___. $\mathscr{C}(R)$ consists of a linear path from $-R$ to R (denoted $l_{[-R,R]}$) and a counter-clockwise oriented semicircle from R back to $-R$ (denoted $\Gamma(R)$). The red curves are where the poles $\tilde{k_z} = \pm K_z = \pm\sqrt{k^2 - k_s^2}$ are located.

The first integral in (2.40) can be solved using the residue theorem. As $R \to \infty$, the pole $\tilde{k_z} = K_z \equiv \sqrt{k^2 - k_s^2}$ will be inside the contour.

$$\begin{aligned}\lim_{R\to\infty} \oint_{\mathscr{C}(R)} \frac{e^{j\tilde{k_z}z}\,\mathrm{d}\tilde{k_z}}{\tilde{k_z}^2 - K_z^2} &= 2\pi j \,\mathrm{Res}_{\tilde{k}_z=K_z}\left(\frac{e^{j\tilde{k_z}z}}{\tilde{k_z}^2 - K_z^2}\right) \\ &= j\frac{\pi e^{jK_z z}}{K_z} \end{aligned} \tag{2.41}$$

Meanwhile, for the second integral:

$$\begin{aligned}\lim_{R\to\infty} \int_{\Gamma(R)} \frac{e^{j\tilde{k_z}z}\,\mathrm{d}\tilde{k_z}}{\tilde{k_z}^2 - K_z^2} &= \lim_{R\to\infty} \int_0^\pi \frac{e^{j(Re^{jt})z}(jRe^{jt}\,\mathrm{d}t)}{(Re^{jt})^2 - K_z^2} \\ &= \lim_{R\to\infty} \frac{j}{R} \int_0^\pi e^{-zR\sin t}\, \frac{e^{j(zR\cos t - t)}}{1 - \frac{K_z^2 e^{-j2t}}{R}}\,\mathrm{d}t \end{aligned} \tag{2.42}$$

As long as $z \geq 0$, this integral goes to zero as $R \to \infty$. Putting these results back into (2.40):

$$\int_{-\infty}^{\infty} \frac{e^{jk_z z}\,\mathrm{d}k_z}{k_z^2 - K_z^2} = j\frac{\pi e^{jK_z z}}{K_z}, \text{ if } z \geq 0 \tag{2.43}$$

To find the solution in the case of $z < 0$, a similar procedure is used except the semicircular is chosen to be $\Gamma'(R) = \{Re^{-jt} \mid 0 \leq t \leq \pi\}$ instead of $\Gamma(R)$, which would be below the k_z-axis in figure 2.6. The other pole $\tilde{k}_z = -K_z$ would be used instead for the residue theorem. The result would be:

$$\int_{-\infty}^{\infty} \frac{e^{jk_z z}\,\mathrm{d}k_z}{k_z^2 - K_z^2} = j\frac{\pi e^{-jK_z z}}{K_z}, \text{ if } z < 0 \tag{2.44}$$

The two results can be combined into one by replacing z with $|z|$:

$$\int_{-\infty}^{\infty} \frac{e^{jk_z z}\,\mathrm{d}k_z}{k_z^2 - K_z^2} = j\frac{\pi e^{jK_z|z|}}{K_z} \tag{2.45}$$

When substituting back into (2.38):

$$\bar{A}(k_s, z) = j\frac{\mu_0 \alpha N I J_1(k_s\alpha) e^{jK_z|z|}}{2K_z} \tag{2.46}$$

Finally, the inverse order-1 Hankel transform, is taken:

$$\begin{aligned} A(s,z) &= \mathcal{H}_1^{-1}\left[\bar{A}\right] \\ &= j\frac{\mu_0\alpha N I}{2} \int_0^\infty \frac{k_s}{K_z(k_s)} J_1(k_s\alpha) J_1(k_s s) e^{jK_z(k_s)|z|}\mathrm{d}k_s \end{aligned} \tag{2.47}$$

Remember that $K_z = \sqrt{k^2 - k_s^2}$. This integral cannot be simplified further without making suitable assumptions to approximate the integral. Note that the denominator in (2.47) will be zero in the case when the coil is in air. If that is the case, one needs to split the integral in two parts in order to properly evaluate numerically (2.47)

By rewriting (2.47) in spherical coordinates instead of cylindrical and assuming that $r = \sqrt{s^2 + z^2} \gg \alpha$, one get:

$$A(s,z) = j\frac{\mu_0 \alpha^2 NI}{4r^2} \int_0^\infty \frac{x^2 e^{j\cos\theta\sqrt{k^2r^2 - x^2}}}{\sqrt{k^2r^2 - x^2}} J_1(x\sin\theta)\mathrm{d}x \tag{2.48}$$

(The substitution $x = k_s\alpha$ was made). This equation agrees with the near-field (2.27) and far field (2.28) equations when the assumptions of $kr \ll 1$ and $kr \gg 1$ are made respectively.

The general magnetic and electric field formulas can now be found from (2.47) using $\mu_0\mathbf{H} = \nabla \times \mathbf{A}$ and $\mathbf{E} = -j2\pi f\mathbf{A}$. The magnetic field is:

$$\mathbf{H} = H_s\hat{\mathbf{s}} + H_z\hat{\mathbf{z}} \tag{2.49a}$$

$$H_s = \frac{NI\alpha}{2} \int_0^\infty k_s J_1(k_s\alpha) J_1(k_s s) e^{jK_z|z|}\mathrm{d}k_s \tag{2.49b}$$

$$H_z = \frac{jNI\alpha}{2} \int_0^\infty \frac{k_s^2}{K_z} J_1(k_s\alpha) J_0(k_s s) e^{jK_w|z|}\mathrm{d}k_s \tag{2.49c}$$

$$K_z = \sqrt{k^2 - k_s^2} \tag{2.49d}$$

The electric field is:

$$E = \pi\mu_0 NI\alpha f \int_0^\infty \frac{k_s}{K_z} J_1(k_s\alpha) J_1(k_s s) e^{jK_w|z|}\mathrm{d}k \tag{2.50}$$

Assuming $z > 0$, (2.49) and (2.50) can be rewritten as:

$$\mathbf{E} = \int_0^\infty E_i(k) J_1(k_s s) e^{jK_z z}\hat{\phi}\ \mathrm{d}k_s \tag{2.51a}$$

$$\mathbf{H} = \int_0^\infty \frac{E_i(k_s)}{2\pi\mu_0 f} \left[K_z J_1(k_s s) e^{jK_z z}\hat{\mathbf{s}} + jk J_0(k_s s) e^{jK_z z}\hat{\mathbf{z}}\right] \mathrm{d}k_s \tag{2.51b}$$

where $E_i(k) = \pi\mu_0 NI\alpha f \frac{k}{K_z} J_1(k_s\alpha)\exp(jK_w d)$. These equations show explicitly the wave structure. This will be important in the next section.

2.4 Solution with the Air-Water Interface

In this section, the solutions for the magnetic will be extended to account for an air-water boundary as shown in Figure 2.7.

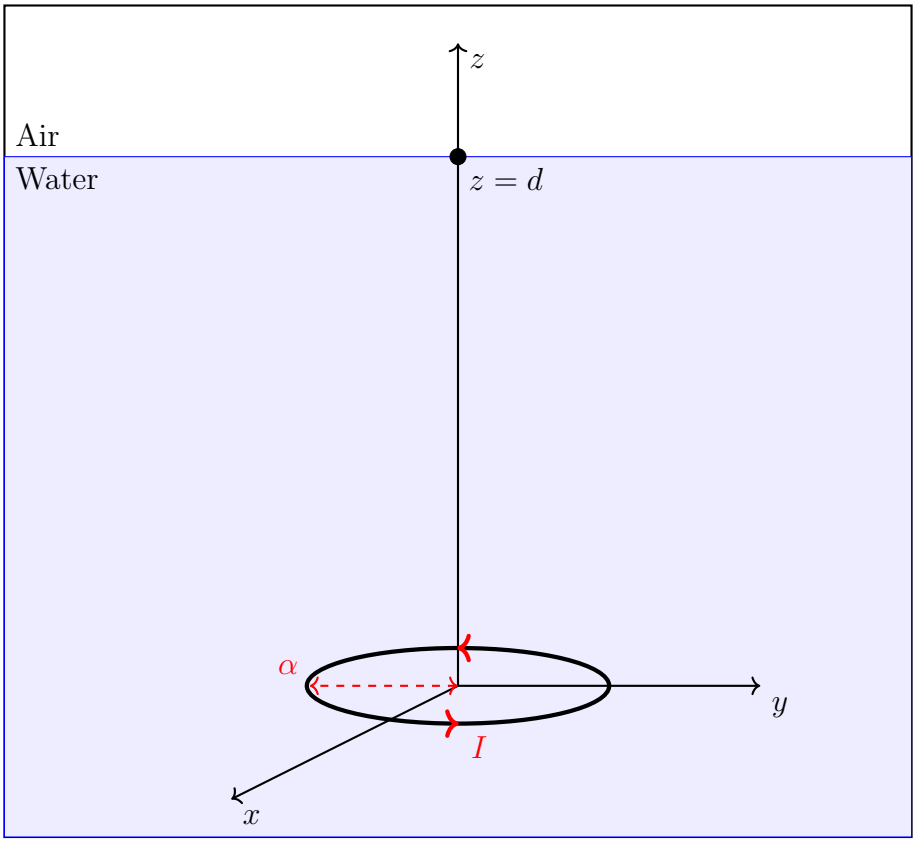

Figure 2.7: Air-water coil configuration

Maxwell's equations are linear in **E** and **H**. Therefore the general solution to (2.5) in a given medium can be written as a linear combination of a homogeneous solution and a particular solution:

$$\mathbf{E} = \mathbf{E}_{homo} + \mathbf{E}_{part} \tag{2.52a}$$

$$\mathbf{H} = \mathbf{H}_{homo} + \mathbf{H}_{part} \tag{2.52b}$$

$\mathbf{H}_{homo}$ and $\mathbf{E}_{homo}$ will solve (2.5) with $\mathbf{J} = 0$.

For the solutions (2.49) and (2.50), one can show that $||\mathbf{H}|| \to 0$ and $||\mathbf{E}|| \to 0$ as $r \to \infty$. Thus these are valid solutions if the coil is in a medium, air or water, that

extends to infinity in all directions, since we can simply set $\mathbf{H}_{homo} = 0$ and $\mathbf{E}_{homo} = 0$. This is a unrealistic scenario, but if other mediums are far enough away, this gives a valid approximation for the fields of a coil.

However, if a second medium is close enough to the coil to have significant impact on the field, (2.49) and (2.50) are not sufficient solutions as in this case $\mathbf{H}_{homo}$ and $\mathbf{E}_{homo}$ cannot be zero. The boundary will introduce an additional 'reflective' component.

First a general structure of $\mathbf{E}_{homo}$ and $\mathbf{H}_{homo}$ is derived while maintaining the assumption of cylindrical symmetry. Let m be an index to indicate which medium. $m = 0$ for air and $m = w$ for water. The general structure of the homogeneous solution in a given medium with permittivity ϵ_m is found by solving (2.5) with $p = 0$ and $\mathbf{J} = 0$, which is equivalent to finding a family of solutions to the wave equations:

$$\nabla^2 \mathbf{E}_{homo} + k_m^2 \mathbf{E}_{homo} = 0 \tag{2.53a}$$

$$\nabla^2 \mathbf{H}_{homo} + k_m^2 \mathbf{H}_{homo} = 0 \tag{2.53b}$$

$$k_m^2 = (2\pi f)^2 \epsilon_m \mu_0 \tag{2.53c}$$

Equation (2.51) implies that cylindrical transverse-electric waves (i.e. cylindrical waves where $\mathbf{E}$ are parallel to the boundary) are the only non-zero solutions to the wave equations for a coil that at a depth d in the water and is parallel to the boundary.

$$\mathbf{E}_{homo} = \int_0^\infty E_m(k_s) J_1(k_s s) e^{jK_z^m z} \hat{\phi} \, \mathrm{d}k_s \tag{2.54a}$$

$$\mathbf{H}_{homo} = \int_0^\infty \frac{E_m(k_s)}{2\pi\mu_0 f} \left[K_z^m J_1(k_s s) e^{jK_z^m z} \hat{\mathbf{s}} + jk J_0(k_s s) e^{jK_z^m z} \hat{\mathbf{z}} \right] \mathrm{d}k_s \tag{2.54b}$$

Here $K_z^m = \sqrt{k_m^2 - k_s^2}$ and k_m is the wavenumber for either air ($m = 0$) or water ($m = w$). The coefficients $E_m(k)$ for $m = 0$ and $m = w$ must be found via the boundary conditions.

Since the air has no sources, $\mathbf{E}$ and $\mathbf{H}$ are only given by the homogeneous solution (2.54) with $m = 0$. In the water (i.e. $z < 0$), $\mathbf{E}$ and $\mathbf{H}$ are given by combining (2.54)

with $m = w$ and (2.51):

$$\mathbf{E} = \int_0^\infty \left[E_i(k) + E_w(k)\right] J_1(k_s s) e^{jK_z^w z} \hat{\phi} \, \mathrm{d}k_s \tag{2.55a}$$

$$\mathbf{H} = \int_0^\infty \frac{E_i(k) - E_w(k)}{2\pi\mu_0 f} \left[K_z^w J_1(k_s s) e^{jK_z^w z} \hat{\mathbf{s}} + jk J_0(k_s s) e^{jK_z^w z} \hat{\mathbf{z}}\right] \mathrm{d}k_s \tag{2.55b}$$

The boundary conditions can be found from the integral form of Maxwell's equations. They are summarized here for a boundary at $z = 0$:

$$\mathbf{E}_\perp^{water} \epsilon_w = \mathbf{E}_\perp^{air} \epsilon_0 \tag{2.56a}$$

$$\mathbf{E}_{||}^{water} = \mathbf{E}_{||}^{air} \tag{2.56b}$$

$$\mathbf{H}^{water} = \mathbf{H}^{air} \tag{2.56c}$$

Apply this to get the following relations:

$$E_w(k) = E_i(k) \frac{K_w(k) - K_0(k)}{K_w(k) + K_0(k)} \tag{2.57}$$

$$E_0(k) = E_i(k) \frac{2K_w(k)}{K_w(k) + K_0(k)} \tag{2.58}$$

Substitute these equations back into (2.55) and (2.54) to get the complete solution for the **H**-field in air ($z > 0$):

$$\mathbf{H} = NI\alpha \int_0^\infty \frac{k_s}{K_z^w + K_z^0} J_1(k_s \alpha) e^{jK_z^w d} \left[K_z^0 J_1(k_s s) e^{jK_z^0 z} \hat{\mathbf{s}} + jk_s J_0(k_s s) e^{jK_z^0 z} \hat{\mathbf{z}}\right] \mathrm{d}k_s \tag{2.59}$$

2.5 Mutual Induction

In this section, mutual inductance is defined (subsection 2.5.1) and its formula is derived for two coils in a single medium (subsection 2.5.2), and in air-water (subsection 2.5.3) just like in figure 2.8. The relationship between mutual induction and the induced voltage in the receiver is discussed in subsection 2.5.4. Finally, a comparison with Wait and Gibson is presented in subsection 2.5.5.

Subscripts TX and RX are added to denote parameters for the transmitter or receiver coils respectively.

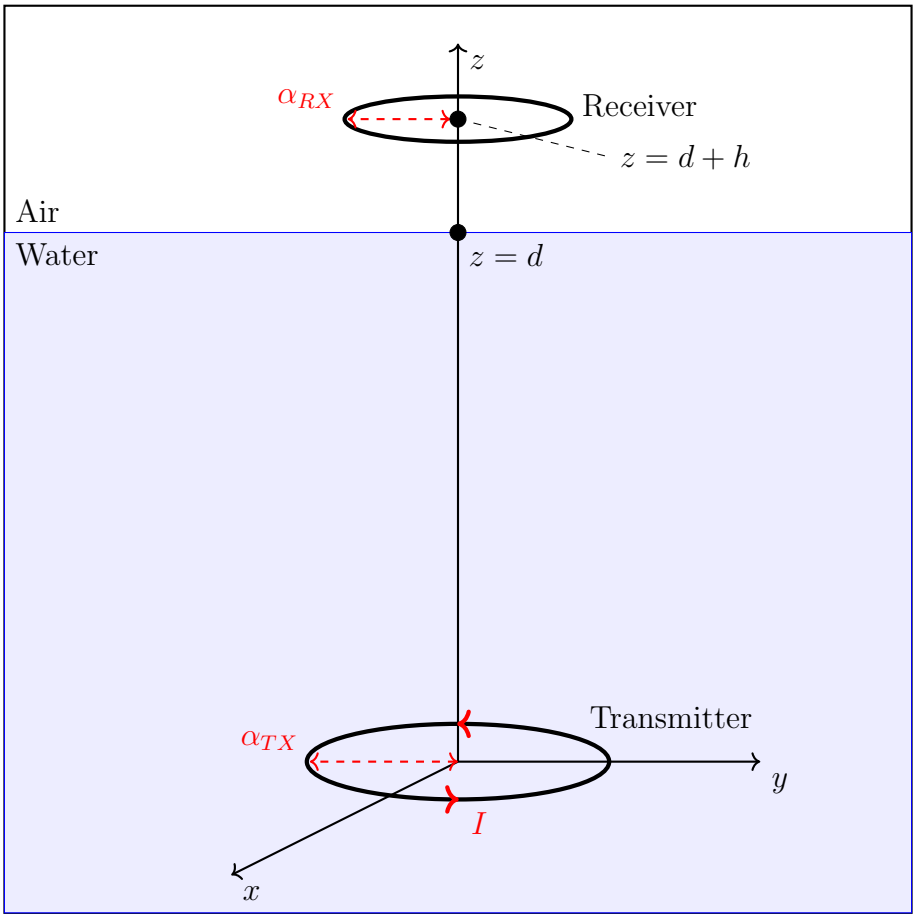

Figure 2.8: Air-water coil configuration for use in deriving the mutual inductance.

2.5.1 Mutual Inductance Definition

Mutual induction is defined as:

$$M(f) = \frac{\mu_0 \Phi_{coil}}{I_{TX}} \tag{2.60}$$

where Φ_{coil} is the magnetic flux across the coil and is given by:

$$\Phi_{coil} = \iint\limits_{\text{coil cross-section}} \mathbf{H} \bullet \mathrm{d}\mathbf{a} \tag{2.61}$$

This equation can be written in a simpler form if $\mathbf{A}$ is known by using $\mu_0 \mathbf{H} = \nabla \times \mathbf{A}$ and Stoke's theorem:

$$\Phi_{coil} = \frac{1}{\mu_0} \int_{coil} \mathbf{A} \bullet \mathrm{d}\mathbf{l} \tag{2.62}$$

Equation (2.62) can be used when there is only one medium, since the vector potential is known via equation (2.47).

2.5.2 Mutual Induction in a Single Medium

To obtain the mutual inductance of two coils in the same medium (air or water), substitute $\mathbf{A}$ with (2.47) and integrate over the receiver coil N_{RX} times. Set $s = \alpha_{RX}$ and $z = d$, the distance between the coils. If one defines the constant term,

$$M_0 = \frac{\pi \mu_0 N_{TX} N_{RX} \alpha_{TX} \alpha_{RX}}{d} \tag{2.63}$$

and the MI ratio function,

$$\mathscr{M}(\Omega, x, y) = j \int_0^\infty \frac{t}{\sqrt{\Omega^2 - t^2}} J_1(xt) J_1(yt) \mathrm{e}^{j\sqrt{\Omega^2 - t^2}} \mathrm{d}t \tag{2.64}$$

the mutual inductance is:

$$M = M_0 \mathscr{M}\left(kd, \frac{\alpha_{TX}}{d}, \frac{\alpha_{RX}}{d}\right) \tag{2.65}$$

where $k = k_0$ for air and $k = k_w(\omega)$ for water. This formula can take a simpler form if suitable conditions are met. In the limit $kd \ll 1$ (or $\Omega \ll 1$), Equation (2.64) reduces to:

$$\mathscr{M}(\Omega, x, y) \approx \mathscr{M}(0, x, y) = \int_0^\infty J_1(xt) J_1(yt) \mathrm{e}^{-t} \mathrm{d}t \tag{2.66}$$

If also $\alpha_{TX}, \alpha_{RX} \ll d$, $\mathscr{M} \approx xy/2$ and:

$$M \approx \frac{\pi \mu_0 N_{TX} N_{RX} \alpha_{TX}^2 \alpha_{RX}^2}{2d^3} \tag{2.67}$$

This is the near-field dipole approximation obtained by calculating the mutual induction to equation (2.27). The strength of the mutual induction in this scenario is inversely proportional to the distance cubed, regardless of the conductivity of the medium.

Alternatively, one can start with the assumption that $\alpha_{TX}, \alpha_{RX} \ll d$ to simplify (2.64):

$$\mathscr{M}(\Omega, x, y) \approx \frac{xy}{4} \bar{\mathscr{M}}(\Omega) \tag{2.68a}$$

$$\bar{\mathscr{M}}(\Omega) = j \int_0^\infty \frac{t^3}{\sqrt{\Omega^2 - t^2}} \mathrm{e}^{j\sqrt{\Omega^2 - t^2}} \mathrm{d}t \tag{2.68b}$$

In the limit $\Omega \ll 1$ (i.e. $kd \ll 1$), M reduces to equation (2.67) as expected. If instead $\Omega \gg 1$ (i.e. $kd \gg 1$):

$$\bar{\mathscr{M}}(\Omega) \approx -2j\Omega \mathrm{e}^{j\Omega} \tag{2.69}$$

This reduces the mutual inductance to become:

$$M \approx -j \frac{\pi \mu_0 k N_{TX} N_{RX} \alpha_{TX}^2 \alpha_{RX}^2}{2d^2} \mathrm{e}^{jkd} \tag{2.70}$$

This is the far-field result from calculating the mutual induction to equation (2.28). In air where k is real, M is inversely proportional to the square of the distance due to field radiation. However in water, k is complex which makes M decay exponentially due to the conductivity of water. This suggests that when setting up a loop MI system, one wants to remain in the near-field to avoid conductivity losses.

To quickly verify the approximations derived above, a numerical evaluation of the reduced MI ratio function $\bar{\mathscr{M}}(\Omega)$ in air with coil separation $d = 20$ meters with the near and far-field limits are shown in figure 2.9. This plot shows that the near-field approximation applies if the frequency is less than 200 kHz and the far-field applies when the frequency is greater than 10 MHz.

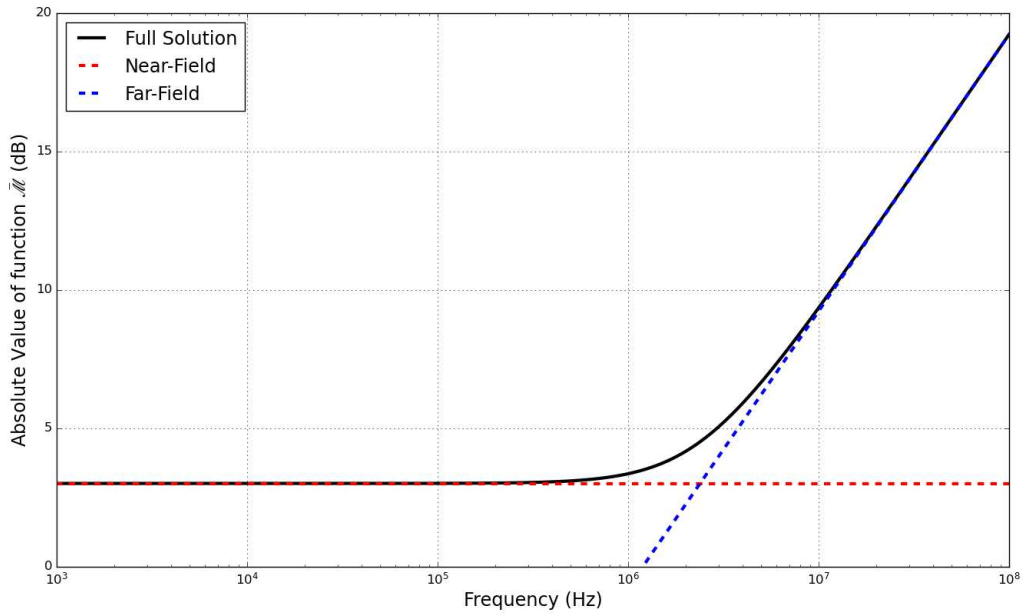

Figure 2.9: Plot of the reduced MI ratio function $\bar{\mathscr{M}}(\Omega)$ defined from equation (2.68a) in air with the near-field and the far-field radiation approximation. The distance between the coils is $d = 20$ m

2.5.3 Mutual Induction with an Air-Water Interface

Since the magnetic field of the air-water configuration is known (equation (2.59)) and not the vector potential, equation (2.61) is applied to find the mutual inductance. In this case, the transmitter is at a depth d and the receiver is at a height h. Define M_0 as in equation (2.63), except replace d with $d + h$. Also define the new MI ratio function:

$$\mathscr{M}(\Omega_w, \Omega_0, x, y, \mathscr{H}) = 2j \int_0^\infty \frac{tJ_1(xt)J_1(yt)}{\sqrt{\Omega_w^2 - t^2} + \sqrt{\Omega_0^2 - t^2}} \, \mathrm{e}^{\left(\frac{1}{1+\mathscr{H}}\sqrt{\Omega_w^2 - t^2} + \frac{\mathscr{H}}{1+\mathscr{H}}\sqrt{\Omega_0^2 - t^2}\right)} \, \mathrm{d}t \tag{2.71}$$

Then the mutual induction becomes:

$$M = M_0 \mathscr{M}\left(k_w(d+h), k_0(d+h), \frac{\alpha_{TX}}{d+h}, \frac{\alpha_{RX}}{d+h}, \frac{h}{d}\right) \tag{2.72}$$

This reduced to (2.65) when $k_w = k_0$ and $h = 0$. If $|k_w|(d+h) \ll 1$ and $k_0(d+h) \ll 1$ equation (2.71) reduces to (2.66) as if there is no medium. Thus the influence on the water conductivity and the boundary only applies in the far field.

If it can be assumed that the coils are far apart from each-other ($\alpha_{TX}, \alpha_{RX} \ll d+h$), then $\mathscr{M}$ can be replaced with:

$$\mathscr{M}(\Omega_w, \Omega_0, x, y, \mathscr{H}) \approx \frac{xy}{4}\bar{\mathscr{M}}(\Omega_w, \Omega_0, \mathscr{H}) \tag{2.73a}$$

$$\bar{\mathscr{M}}(\Omega_w, \Omega_0, \mathscr{H}) = j\int_0^\infty \frac{t^3}{\sqrt{\Omega_w^2 - t^2} + \sqrt{\Omega^2 - t^2}} \mathrm{e}^{\left(\frac{1}{1+\mathscr{H}}\sqrt{\Omega_w^2 - t^2} + \frac{\mathscr{H}}{1+\mathscr{H}}\sqrt{\Omega_0^2 - t^2}\right)} \mathrm{d}t \tag{2.73b}$$

As expected, this equation reduces to the near-field model (2.67) with d replaced with $d+h$ when $|\Omega_w| = |k_w|(d+h) \ll 1$ and $\Omega_0 = k_0(d+h) \ll 1$. In the opposite limit $|k_w|(d+h) \gg 1$ and $k_0(d+h) \gg 1$, one gets a different far-field model:

$$M \approx -j\frac{\pi\mu_0 k_w^2 k_0^2 N_{TX} N_{RX} \alpha_{TX}^2 \alpha_{RX}^2}{2(k_w + k_0)(k_w h + k_0 d)^2} \mathrm{e}^{j(k_w d + k_0 h)} \tag{2.74}$$

This model reduces to the far-field model in only one medium (equation (2.70)) if $k_w = k_0$ and $h = 0$. Since k_w is complex, this model has exponential decay with the depth d of the transmitter, but not with the height h of the receiver which behaves as an inverse squared relation as if there is radiation. Thus the fields decay in the water but then acts like a radiation field when they cross the boundary to the air.

Note that from equation (2.3), $|\epsilon_w| = \sqrt{81^2\epsilon_0^2 + (\sigma/2\pi f)^2} \geq 81\epsilon_0 \gg \epsilon_0$ which implies that $|k_w| \gg |k_0|$. Thus there exists a third intermediate-field when $1/|k_w| \ll d + h \ll 1/k_0$ (or $|\Omega_w| \gg 1$ and $\Omega_0 \ll 1$). In this new intermediate-field, the mutual induction from (2.72) can be approximated by:

$$M \approx -j\frac{\pi\mu_0 k_w d N_{TX} N_{RX} \alpha_{TX}^2 \alpha_{RX}^2}{(d+h)^3} \mathrm{e}^{jk_w d} \tag{2.75}$$

Note that the receiver coil height h behaves like a 'near-field' with the inverse cube, but the transmitter depth d behaves like a 'far-field' with the exponential decay term.

A sample plot of the reduced MI ratio function $\bar{\mathscr{M}}$ from equation (2.73a) versus frequency for a transmitter of depth $d = 19$ meters and a receiver of height $h = 1$ meter (thus $d + h = 20$ meters) is shown in figure 2.10 along with all three approximations presented in this section. The near-field applies as long as $f < 1$ kHz after which the decay from the conductivity of water takes in effect. Both the intermediate-field and the far-field in this scenario are indistinguishable and both model the system when $f > 4$ MHz.

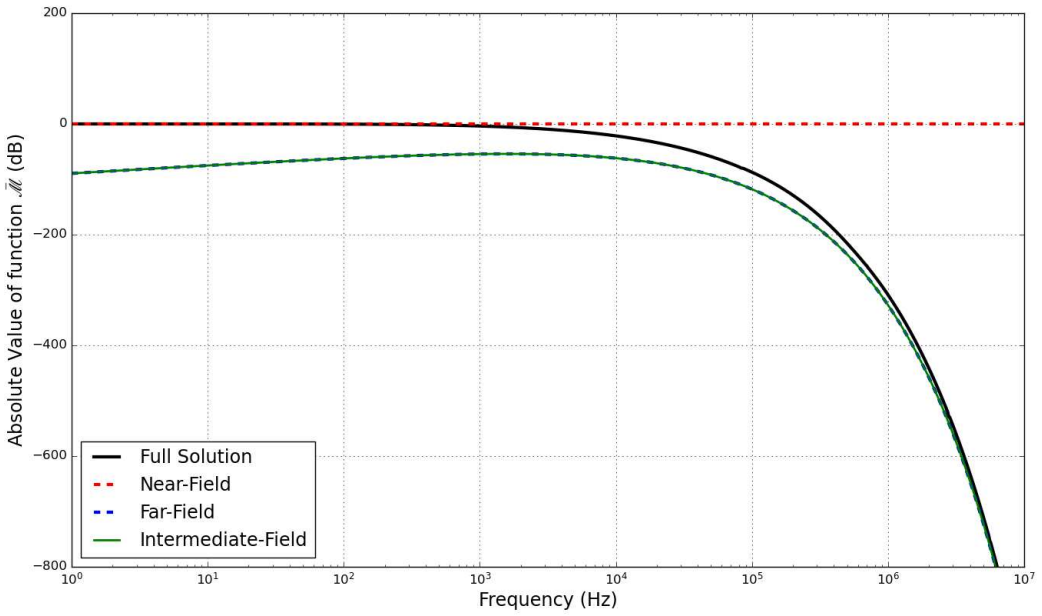

Figure 2.10: Plot of the reduced MI ratio function $\bar{\mathscr{M}}(\Omega_w, \Omega_0, \mathscr{H})$ defined from equation (2.73a) in air with the near-field, the far-field, and the intermediate-field approximations. The TX depth is $d = 19$ m and the height $h = 1$ m.

2.5.4 Induced Voltage

When analysing the effect of the mutual inductance, what is important is the induced voltage on the receiver from the changing magnetic field created from the transmitter. In the frequency domain, the relationship between the induced voltage V_{ind} in the receiver from a transmitter with fixed current I_{TX} is:

$$V_{ind}(f) = -j2\pi f M I_{IX} \tag{2.76}$$

Here, M is the mutual inductance. If the system is in a medium with conductivity, then M is a complex number and is a function of frequency f. The real part of M is responsible for power delivery from the transmitter to the receiver whereas the imaginary part behaves like an extra impedance term which dissipates power.

As $f \to 0, V_{ind} \to 0$ as one would expect since there would be no induction with static currents. In air-water, the exponential decay also ensures that as $f \to \infty, V_{ind} \to 0$ as well. Therefore there is a frequency where the induced voltage is at a

maximum. This maximum would depend on the coil separation d, h and is predicted to get smaller as the separation is larger.

Define the function $\mathscr{F}(f)$ by:

$$\mathscr{F}(f) = \left| 2\pi f \frac{M(f)}{M_0} \frac{(d+h)^2}{\alpha_{TX}\alpha_{RX}} \right| \tag{2.77}$$

Thus $|V_{ind}/I_{TX}| = \mathscr{F}(f)$ and can be interpreted as a normalized voltage-to-current ratio. This is plotted as a function of frequency in figure 2.11 using equation (2.72) for the mutual inductance with the receiver at a height $h = 1$ meter and the transmitter at depths $d = 10$, 25, 50, and 100 meters. One can see that the frequency of operation to maximize V_{ind}/I_{TX} gets smaller very quickly as the transmitter coil goes deeper underwater.

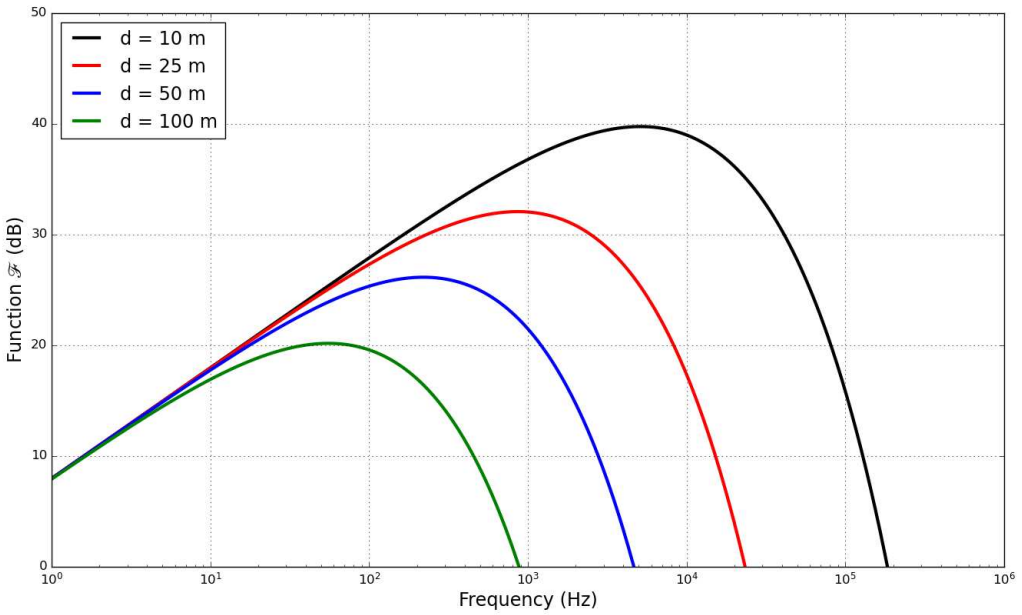

Figure 2.11: Plot of the normalized induced voltage over transmitter current $\mathscr{F}$ function defined in equation (2.77) versus frequency for a fixed RX coil height of 1 meter and various TX coil depths.

2.5.5 Comparison with Gibson's Results

In this section, the model from Wait and Gibson [6] will be compared with the full mutual inductance model derived in equation (2.72):

$$M_{Gibson} = \frac{\pi\mu_0 N_{TX} N_{RX} \alpha_{TX}^2 \alpha_{RX}^2}{2d^3} \int_0^\infty \frac{x^3 e^{-\left(x\frac{h}{d}+\sqrt{x^2+j2\pi\mu_0 hf\sigma}\right)}}{x+\sqrt{x^2+j2\pi\mu_0 hf\sigma}} \mathrm{d}x \tag{2.78}$$

In this situation, the receiver coil is placed 1 meter above the surface and the transmitter coil is 19 meters deep underwater. Both the new model and Wait's model for the magnetic induction agree with the near-field model at frequencies much less than 1 kHz. The new model begins to decay much sooner than Wait-Gibson model, which remains constant until approximately 1 MHz before it begins to decay exponentially. This suggests that the Wait-Gibson model does not apply to this air-water antenna system.

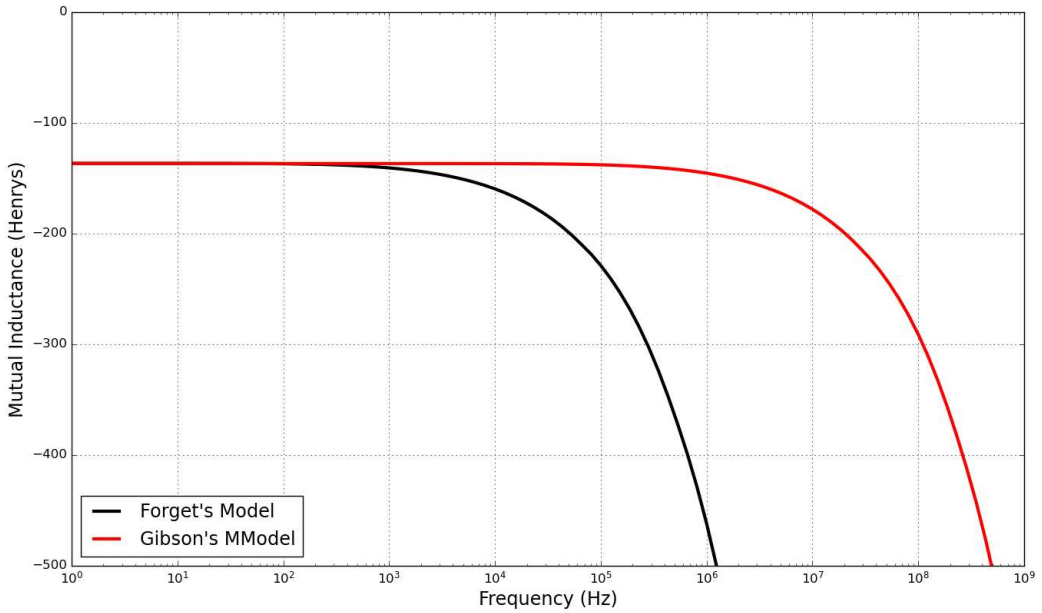

Figure 2.12: Plot of Magnetic Induction in air-water from equation (2.72) and from Wait's (2.78).

2.6 Circuit Analysis

In this section, circuits for the transmitter (subsection 2.6.1) and receiver (subsection 2.6.2) are included to analyze the voltage ratio expected using the models for the mutual inductances above. It is assumed that the mutual inductance is given by the models described by equations (2.65-2.72), depending on what medium the coils are in. Subsection 2.6.3 investigates the influence of a capacitor added to the receiver. Finally, subsection 2.6.4 briefly discuses whenever a passive repeater can improve the voltage ratio.

2.6.1 Transmitter Circuit Model

The goal of the transmitter circuit is to have as close as possible to a frequency-independent relationship with the current I_{TX} powered in the circuit. This is because the power transferred to the receiver is directly proportional to the current in the transmitter. At large frequencies, the self-inductance of the coil behaves like a large impedance and reduces the maximum possible current.

The circuit diagram for the transmitter is given in figure 2.13. All components are chosen to be in series. The TX coil is assumed to have a self-inductance L_{TX} and a parasitic resistance R_{TXpar}. The coil is powered by a voltage source which will be assumed to be sinusoidal with amplitude V_{in} and frequency f. A fixed resistor R_{TX} is added to measure the current and to influence the current profile as will be shown shortly.

It is assumed that the coils are far enough apart such that the induction from the receiver back to the transmitter is negligible. Thus the equation for the transmitter circuit is:

$$V_{in} - (R_{TX} + R_{TXpar} + j2\pi f L_{TX})I_{TX} = 0 \tag{2.79}$$

Solving for I_{TX} gives:

$$I_{TX} = \frac{I_{TX}^{DC}}{1 + j\frac{f}{f_{cut}}} \tag{2.80}$$

where the DC limit current is defined by $I_{TX}^{DC} = V_i/(R_{TX} + R_{TXpar})$ and the cut-off frequency is $f_{cut} = (R_{TX} + R_{TXpar})/2\pi L_{TX}$. The relationship between the current

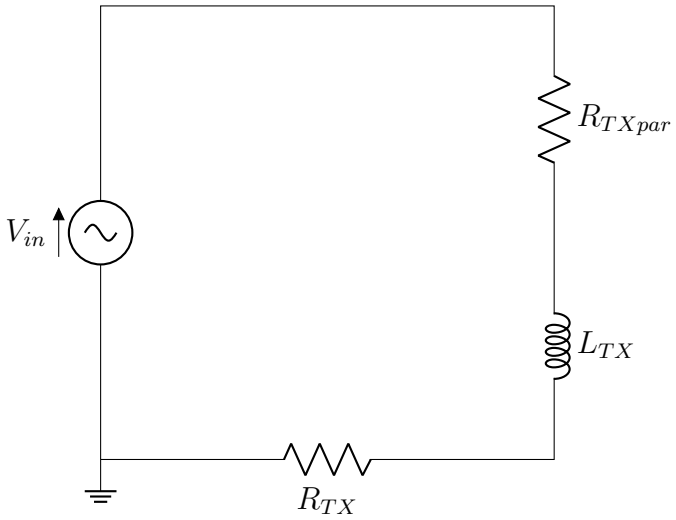

Figure 2.13: Circuit diagram for the transmitter coil.

and the frequency is a low-pass filter with the maximum possible current being I_{TX}^{DC} and the cutoff frequency being f_{cut}. Because of the presence of parasitic resistance in the coil, the DC current limit can be no larger than V_i/R_{TXpar}. By increasing R_{TX}, the maximum current goes down, but the cutoff frequency increases which means one can operate at larger frequencies. Figure 2.14 demonstrates the relationship between I_{TX} with f and how R_{TX} affects the shape of the plot.

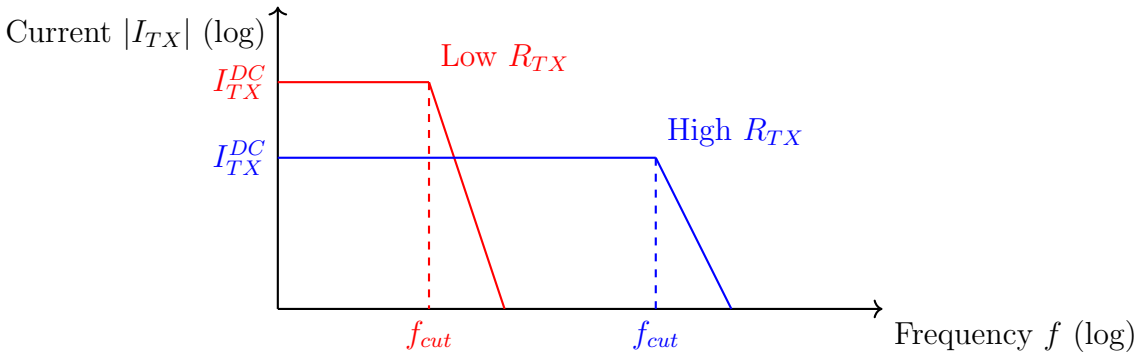

Figure 2.14: Plot showing the relationship between the amplitude of the transmitter current $|I_{TX}|$ with frequency and how it is affected by the presence of a resistor R_{TX}.

2.6.2 Receiver Circuit Model with no Capacitor

In the following, a receiver with a load resistance R_{RX} is considered and the analysis conducted of how a transmitter with current I_{TX} induces a voltage across the load V_{out}. Figure 2.15 shows the circuit diagram of a receiver coil in series with a load resistance. The coil receives an induced voltage $-j2\pi fMI_{TX}$ from the transmitter, but has an impedance from its self-inductance L_{RX} and parasitic resistance R_{RXpar}.

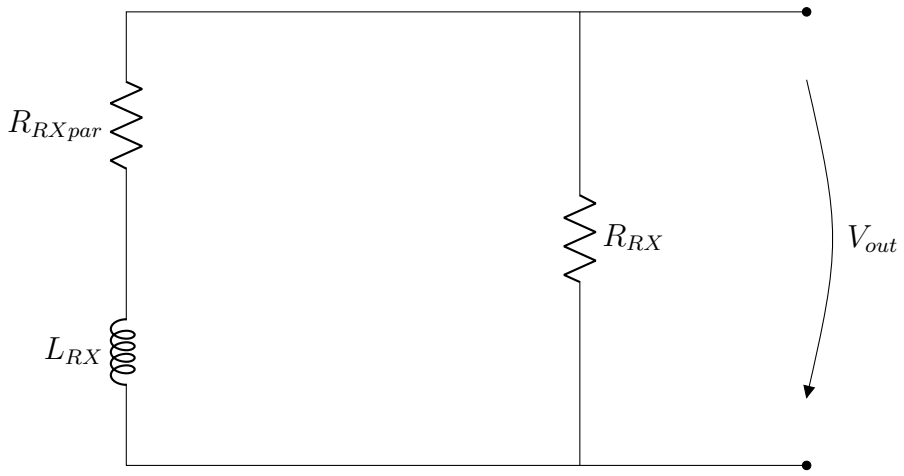

Figure 2.15: Circuit diagram for the receiver coil.

The load voltage V_{out} is related to the receiver current I_{RX} in two ways:

$$V_{out} = R_{RX}I_{RX} \tag{2.81a}$$

$$V_{out} = -j2\pi MI_{TX} - (j2\pi L_{RX} + R_{RXpar})I_{RX} \tag{2.81b}$$

Define the voltage across the transmitter fixed voltage to be $V_{R_{TX}} = R_{TX}I_{TX}$. Solving for V_{out} and the divide by $V_{R_{TX}}$ to get the voltage ratio $\mathscr{V}(f)$:

$$\mathscr{V}(f) = \frac{V_{out}}{V_{R_{TX}}} = \frac{jfA}{1 + j\frac{f}{f_l}} \tag{2.82}$$

where the constant term A (in units of seconds) is defined by:

$$A = \frac{2\pi MR_{TX}}{1 + \frac{R_{RXpar}}{R_{RX}}} \tag{2.83}$$

and the frequency term f_l is defined by:

$$f_l = \frac{R_{RX}}{2\pi L_{RX}}\left(1 + \frac{R_{RXpar}}{R_{RX}}\right) \tag{2.84}$$

As figure 2.16 shows, $\mathscr{V}$ is a high-pass filter with cutoff-frequency f_l and maximum value of $f_l A$. If $f \ll f_l$, the voltage ratio is linear with frequency whereas if $f \gg f_l$, the voltage ratio is fixed at the maximum value. Ideally one wants $R_{RX} = 0$, but that is unrealistic as one wants to connect a load to the system. If possible, choose frequencies larger than f_l.

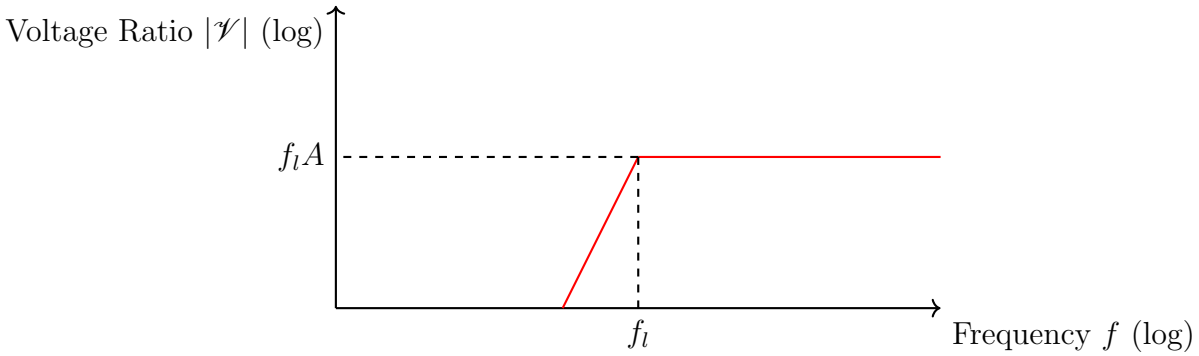

Figure 2.16: Plot showing the relationship between the amplitude of the voltage ratio $\mathscr{V}$ from equation (2.82) with frequency.

The key observation to make is that the constant A, which determines the maximum voltage ratio, is proportional to the mutual inductance M. One can measure M from the maximum of $\mathscr{V}$.

2.6.3 Receiver Circuit Model with a Capacitor

To improve the measured voltage, one can consider adding a capacitor C_{RX} in parallel to the load. The new circuit diagram looks like figure 2.17: The load is now $Z_{RX} = R_{RX}||(1/j2\pi f L_{RX})$. Replace R_{RX} with Z_{RX} in equation (2.81 to obtain the new voltage ratio:

$$\mathscr{V}(f) = \frac{V_{out}}{V_{R_{TX}}} = \frac{jfA}{1 - \frac{f^2}{f_0^2} + j\frac{f}{f_l}} \tag{2.85}$$

This equation looks like (2.82) except it now has a new term in the denominator. A is the same as in (2.83). However f_l is now defined by:

$$f_l = 2\pi \frac{1 + \frac{R_{RXpar}}{R_{RX}}}{\frac{L_{RX}}{R_{RX}} + R_{RXpar} C_{RX}} \tag{2.86}$$

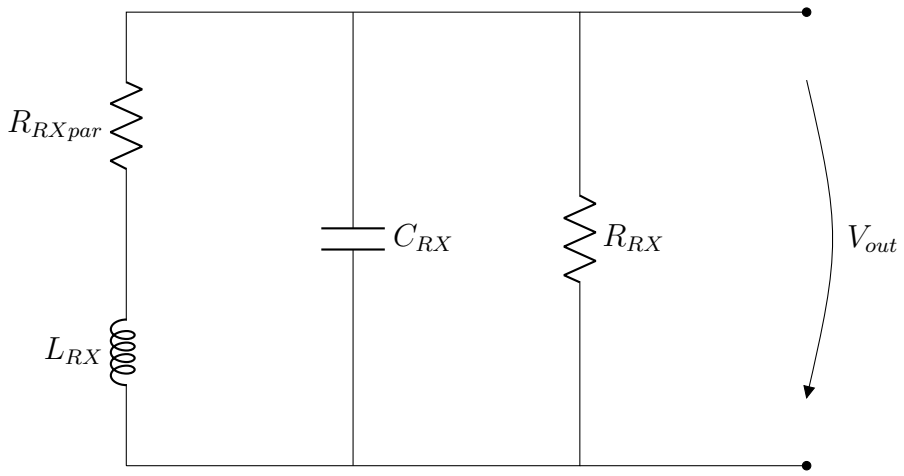

Figure 2.17: Circuit diagram for the receiver coil with a capacitor in parallel.

The resonance frequency is given by:

$$f_0 = \frac{1}{2\pi}\sqrt{\frac{1+\frac{R_{RXpar}}{R_{RX}}}{L_{RX}C_{RX}}} \tag{2.87}$$

Near the resonance frequency the voltage ratio will be larger than if no capacitors are present. However at frequencies far away from the resonance frequency, the voltage ratio is smaller. Thus adding a capacitor is useful if there is a specific frequency in particular one wants to operate.

2.6.4 Repeater Circuit

Domingo [2] proposes to use a sequence of passive repeater coils in between the antenna arrays in order to create a waveguide for the induced magnetic fields and thus improve the performance. But having too many repeater coils defeats the purpose of having a coil antenna system. Thus the feasibility of using a single repeater coil is investigated.

Consider a repeater coil a distance d_r above the transmitter and thus $d - d_r$ below the receiver as in figure 2.18. The repeater coil has a radius α_r and has N_r turns. Under what conditions does the repeater help with the transmission loss?

It should be noted that the repeater cannot be a simple coil with no components.

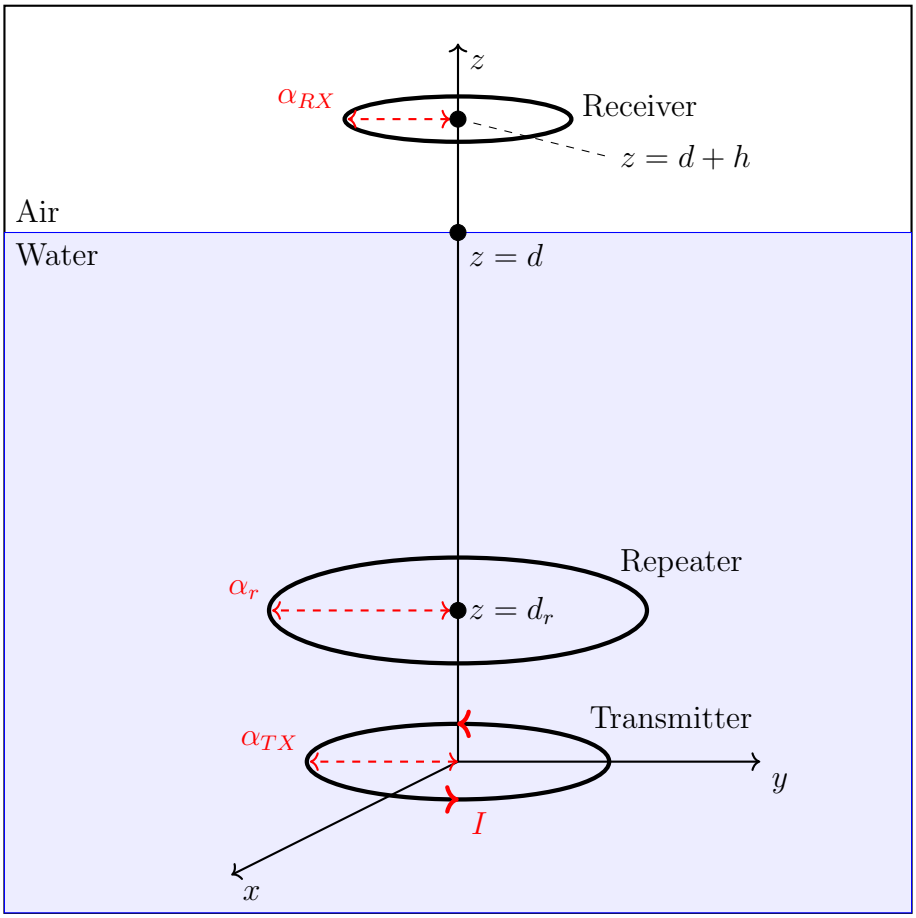

Figure 2.18: Air-water repeater configuration.

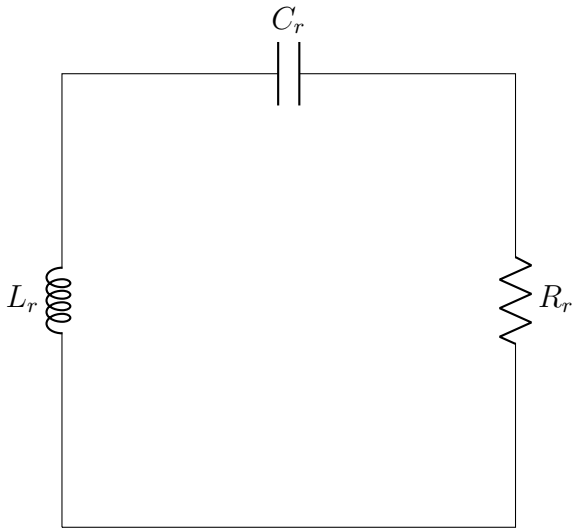

Figure 2.19: Circuit diagram for the repeater coil.

Faraday's law states that the voltage in the repeater will always be 180° out of phase relative to the transmitter. If there are no capacitors in the repeater, the current in the repeater will also be 180° out of phase and thus creates a magnetic field that reduces the field of the transmitter. Therefore a capacitor is needed in the repeater to change the phase.

The circuit for the repeater is given by figure 2.19. The self-inductance is L_r, the capacitance is C_r, and the resistor is R_r (which is simply the resistance of the wire). Define $Z_r = R_r + j2\pi f L_r - j/2\pi f C_r$.

Denote M_{TR} for the mutual inductance between the transmitter and the receiver, M_{Tr} for the mutual inductance between the transmitter and the repeater, and M_{rR} for the mutual inductance between the receiver and the repeater. The circuit equation for the repeater is:

$$-Z_r I_r - j2\pi f M_{Tr} I_{TX} - j2\pi f M_{rR} I_{RX} = 0 \tag{2.88}$$

The circuit equation for the receiver, now with a repeater, becomes:

$$-Z_{RX} I_{RX} - j2\pi f M_{TR} I_{TX} - j2\pi f M_{rR} I_r = 0 \tag{2.89}$$

Here, $Z_{RX} = j2\pi f L_{TX} + \frac{1}{\frac{1}{R_{RX}} + j2\pi f C_{RX}}$. If I_{TX} is fixed and $V_{R_{TX}} = R_{TX} I_{TX}$ is how

to measure the current, the new voltage ratio is:

$$\mathscr{V}_{\text{With Repeater}}(f) = \frac{R_{TX}(-4\pi^2 f^2 M_{Tr} M_{rR} - j2\pi f Z_r MTR)}{\left(\frac{1}{R_{RX}} + j2\pi f C_{RX}\right)(Z_r Z_{RX} + 4\pi^2 f^2 M_{rR}^2)} \tag{2.90}$$

This reduces to the old voltage ratio with capacitors from equation (2.85) if $|Z_r| \to \infty$ (i.e. the repeater becomes an open circuit).

To verify if the repeater makes a difference or not, a numerical contour plot of the ratio of equation (2.90) with (2.85) as a function of both the repeater position d_r between the antenna coils and the repeater coil radius α_r is created. The distance between the TX and RX is chosen to be 25 meters and the frequency is fixed to 1 kHz since figure 2.11 suggest that 1 kHz gives the best performance for antenna coils 25 meters apart. C_r, C_{RX} are chosen to resonate the system at 1 kHz, and the resistances are chosen to be: $R_{TX} = 1\Omega, R_r = 0.1\Omega, R_{RX} = 1\text{k}\Omega$. Knowledge of L_r is not needed since at resonance the impedance from L_r will be cancelled by C_r. L_{RX} needs to be known and will be related to parameters to the RX coil. The value of L_{RX} will be estimated using the following formula from [19]:

$$L_{RX} = \mu_0 N_{RX}^2 \alpha_{RX} \left[\ln\left(\frac{8\alpha_{RX}}{a_{RX}}\right) - 2\right] \tag{2.91}$$

Here, a_{RX} is the radius to the wire used. It is chosen to be 1 mm. At 1 kHz frequency, the system is in the near-field and the properties of the mediums can be ignored.

The contour plot of the ratio of voltage ratios (2.90) with (2.85) is given in figure 2.20. If the repeater is around the same size or smaller than the antenna coils, there is no difference. For a change in the voltage ratio, the repeater must be at least 10 times larger than the antenna coil, and be very close to the transmitter. If the repeater is further away, it must be 100 times larger and no further than half-way between the coils. If the repeater is too close to the receiver, the voltage ratio is worse than having no repeater.

In conclusion, the use of a single passive repeater is not practical since either the coil would have to be very close to the transmitter to improve the power transfer (which could be easily achieve by increasing the turn ratio of the antenna coils), or the coil must unreasonably large.

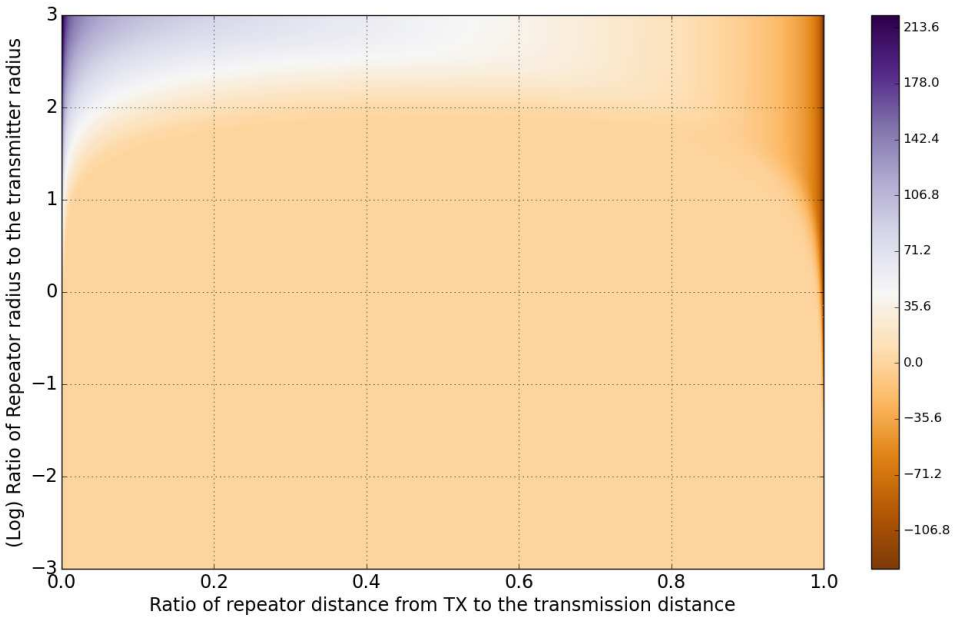

Figure 2.20: Contour plot (in decibels) of the ratio $\mathscr{V}_{\text{With Repeater}}/\mathscr{V}_{\text{No Repeater}}$ from equations (2.90) and (2.85) as a function of the ratio of repeater distance to antenna distance and the ratio of repeater radius to transmitter radius.

Chapter 3

MI Link Measurements

This chapter provides an overview of the equipment and how it was used in the experiments. Section 3.1 details the equipment, section 3.2 explains how the mutual induction measurements were performed in air at the lab, and section 3.3 presents the setup at the Dalhousie Aquatron for the air-water test.

3.1 Equipment

The equipment consisted of a transmitter coil, a receiver coil, an impedance analyzer, resistors, capacitors, power supplies, a power amplifier, a signal generator, an oscilloscope, a low-noise amplifier, and an inverting amplifier.

3.1.1 Transmitter and receiver coils

The transmitter coil is shown in figures 3.1 and 3.2. There are three independent coils that are mutually orthogonal, which allows the choice of orientation to induce a magnetic field. All coils are wrapped around a green plastic shell with groves to hold the coils in place. A larger black plastic shell is made to cover and seal the coil from water with a small opening for the wires. The transmitter wires are long and covered by a thick cable to protect them from water. Each coil is color coded blue, green, or yellow, to mark which pair of wires correspond to which coil. Colored green and yellow tapes on the exterior shell help find the correct orientation and the corresponding wire with the same color. The blue wire corresponds to the coil oriented along the seal.

The coils have a diameter of 13 centimeters and have approximately 35 turns. The impedances of the three coils were measured using a Hewitt-Packard 4192A LF Impedance Analyzer (figure 3.3), and are summarized in Table 3.1, Table 3.2, and

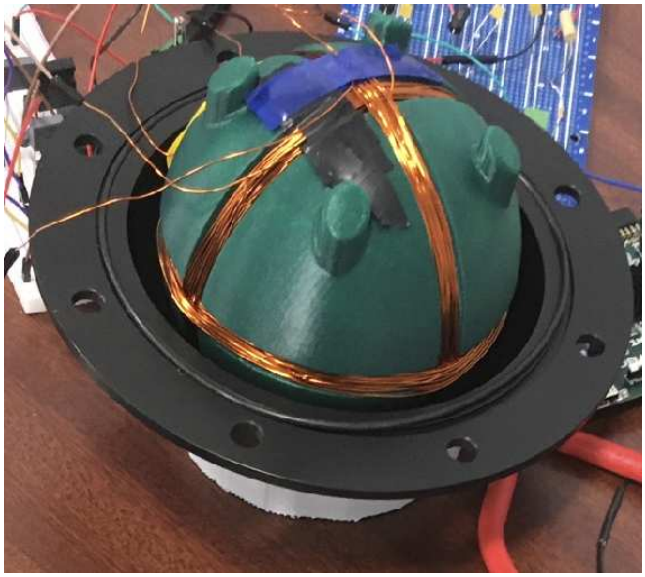

Figure 3.1: Image of the transmitter with the exterior open.

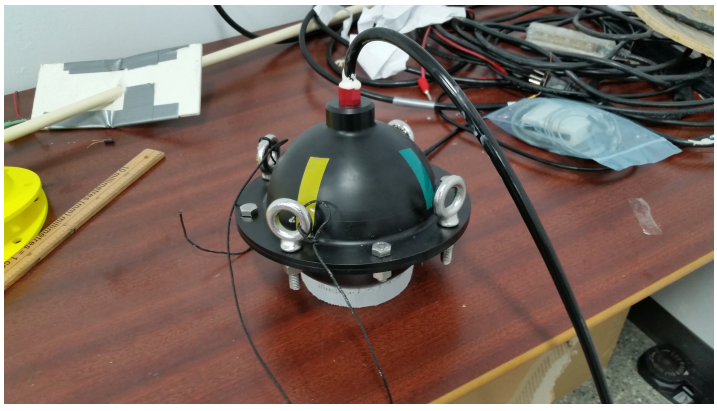

Figure 3.2: Image of the transmitter with the exterior closed. The yellow and green tapes show the coil orientations.

Table 3.3.

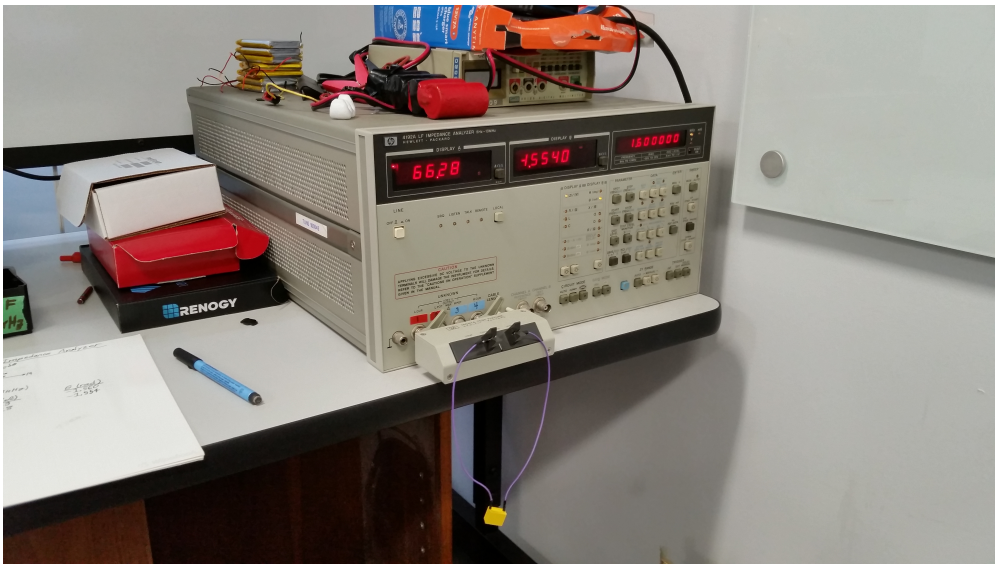

Figure 3.3: Image of the Hewitt-Packer 4192A LF Impedance Analyzer used to measure the impedances of all coils and capacitors.

The receiver coil is shown in figure 3.4. It is a single coil wrapped around green plastic housing, and similar to transmitter, the signal travels a long water-resistant cable. Since the receiver will not be underwater, an external case is not needed. The impedance is measured with the same impedance analyzer as in figure 3.3. The resulting data is shown in table 3.4.

3.1.2 Resistors and Capacitors

There are three independent copies of the circuit designed as in figure 2.13, which allows each transmitter coil to operate independently of one another. The resistors in each circuit are all at 5 Ohms and are designed to carry a current of 1 to 2 Amperes without risk of damage due to a large heatsink to dissipate the heat. The location of the power amplifier is also shown.

The receiver circuit is designed to replicate figure 2.17. The resistances are each 5 Ohms or 120 Ohms and a capacitor can be added in parallel. Also shown is the

f (kHz)	$\|Z\|(\Omega)$	θ (raians)	$R(\Omega)$	$X(\Omega)$	$L(\mu H)$
1.0	4.9	0.352	4.60	1.69	269
1.6	5.3	0.532	4.57	2.69	267
2.5	6.2	0.743	4.57	4.19	267
4.0	8.1	0.971	4.57	6.61	266
6.3	11	1.16	4.39	10.1	255
10	17	1.30	4.55	16.4	261
16	27	1.40	4.59	26.6	265
25	42	1.45	5.06	41.7	265
40	67	1.49	5.41	66.8	266
63	110	1.51	6.68	110	277
100	170	1.52	8.63	170	270
160	310	1.53	12.6	310	308
250	640	1.54	19.7	640	407

Table 3.1: Table of the impedance values of the TX coil labeled green. The frequency is f, the impedance is $Z = |Z| \exp(j\theta) = R + jX$, and the self-inductance is L.

f (kHz)	$\|Z\|(\Omega)$	θ (radians)	$R(\Omega)$	$X(\Omega)$	$L(\mu$H)
1.0	4.9	0.347	4.61	1.67	265
1.6	5.3	0.525	4.59	2.66	264
2.5	6.2	0.735	4.60	4.16	265
4.0	8.1	0.964	4.62	6.65	265
6.3	11	1.15	4.49	10.0	254
10	17	1.30	4.55	16.4	261
16	27	1.39	4.89	26.6	264
25	42	1.45	5.06	41.7	265
40	67	1.49	5.41	66.8	266
63	110	1.51	6.68	110	277
100	170	1.52	8.63	170	270
160	310	1.53	12.6	310	308
250	650	1.54	20.0	650	414

Table 3.2: Table of the impedance values of the TX coil labeled yellow. The frequency is f, the impedance is $Z = |Z| \exp(j\theta) = R + jX$, and the self-inductance is L.

f (kHz)	$\|Z\|(\Omega)$	θ (raians)	$R(\Omega)$	$X(\Omega)$	$L(\mu\text{H})$
1.0	4.7	0.359	4.40	1.65	263
1.6	5.1	0.541	4.37	2.63	261
2.5	6.0	0.752	4.38	4.10	261
4.0	7.9	0.980	4.40	6.56	261
6.3	11	1.17	4.29	10.1	256
10	17	1.31	4.38	16.4	261
16	27	1.40	4.59	26.6	265
25	41	1.46	4.53	40.7	269
40	66	1.49	5.33	65.8	262
63	100	1.51	6.08	99.8	252
100	170	1.52	8.63	170	270
160	300	1.53	12.2	300	298
250	620	1.54	19.1	620	395

Table 3.3: Table of the impedance values of the TX coil labeled blue. The frequency is f, the impedance is $Z = |Z|\exp(j\theta) = R + jX$, and the self-inductance is L.

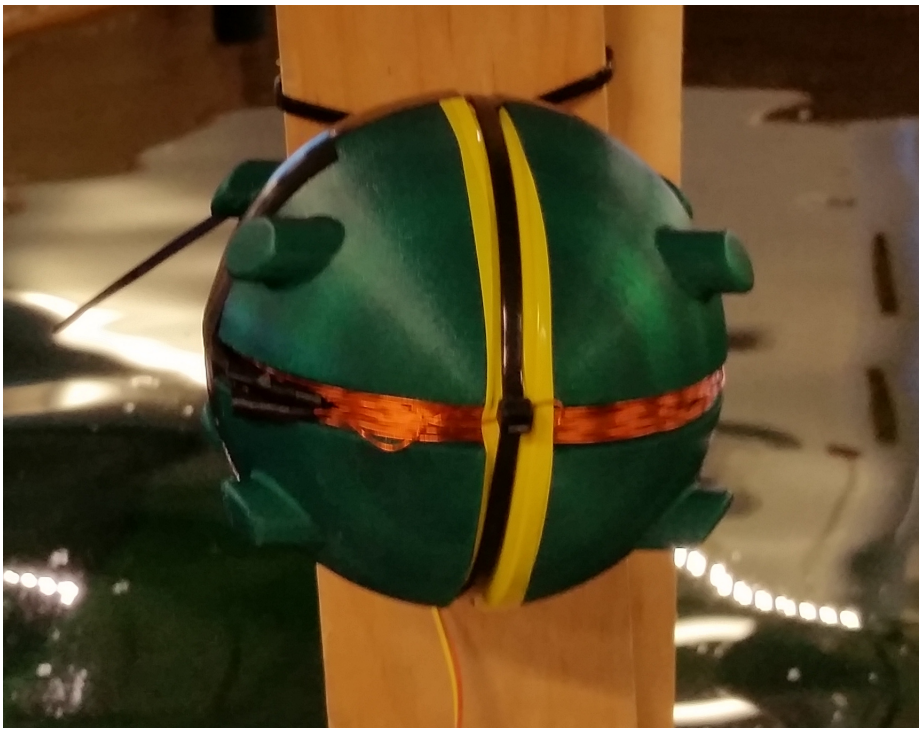

Figure 3.4: Image of the Receiver.

f (kHz)	$\|Z\|(\Omega)$	θ (raians)	$R(\Omega)$	$X(\Omega)$	$L(\mu\text{H})$
1.0	3.6	0.553	3.06	1.89	301
1.6	4.2	0.779	2.99	2.95	294
2.5	5.6	0.995	3.05	4.70	299
4.0	8.0	1.18	3.05	7.40	294
6.3	12	1.32	2.98	11.6	294
10	19	1.41	3.04	18.8	298
16	30	1.46	3.32	29.8	297
25	47	1.50	3.32	46.7	298
40	75	1.52	3.81	74.9	298
63	120	1.53	4.89	120	303
100	190	1.53	7.75	190	302
160	330	1.54	10.2	330	328
250	610	1.54	18.8	610	388

Table 3.4: Table of the impedance values of the RX coil. The frequency is f, the impedance is $Z = |Z|\exp(j\theta) = R + jX$, and the self-inductance is L.

series of operational amplifiers in order to measure the signal.

The choice of capacitor in the receiver is 15 μF which allows for a resonance frequency of 8 kHz. The capacitor value is verified using the impedance analyser. Tables 3.5 gives the measured impedance of the capacitor using the HP impedance analyzer in figure 3.3.

f (kHz)	$\|Z\|(\Omega)$	θ (radians)	$R(\Omega)$	$X(\Omega)$	$C(\mu\text{F})$
1.0	110	-1.56	1.19	-110	1.45
1.6	66	-1.55	1.37	-66.0	1.51
2.5	42	-1.55	0.873	-42.0	1.52
4.0	26	-1.54	0.801	-26.0	1.53
6.3	17	-1.52	0.863	-17.0	1.49
10	11	-1.49	0.888	-11.0	1.45
16	6.6	-1.45	0.795	-6.55	1.52
25	4.2	-1.39	0.755	-4.13	1.54

Table 3.5: Table of the impedance values of the 15 μF capacitor used to resonate at 8 kHz. The frequency is f, the impedance is $Z = |Z|\exp(j\theta) = R + jX$, and the capacitance is C.

3.1.3 Power supply, power amplifier, and signal generator in the transmitter

The purpose of the power amplifier is to provide a consistent current in the range of 1 A, regardless of what source is used to generate sinewaves. A Figure 3.5, and **??** the power amplifier (APEX EVAL68 rev. B) used for this experiment. It is chosen because it provides linear amplification for an output current as high as 1 Amp in the frequency band of interest. A RIGOL DP832A DC power supply is used to power the circuit and the RIGOL DG4162 signal generator is used to apply the transmitter with a sinewave at a given frequency. The power amplifier accept a DC power supply voltage of ±15 Volts, and can accept a peak-peak voltage from the signal generator of up to 5 Volts and a frequency less than 25 kHz, after which the power amplifier introduces nonlinear signals in the circuit. The internal resistance of the power amplifier varies between 3 to 5 Ohms depending of the frequency.

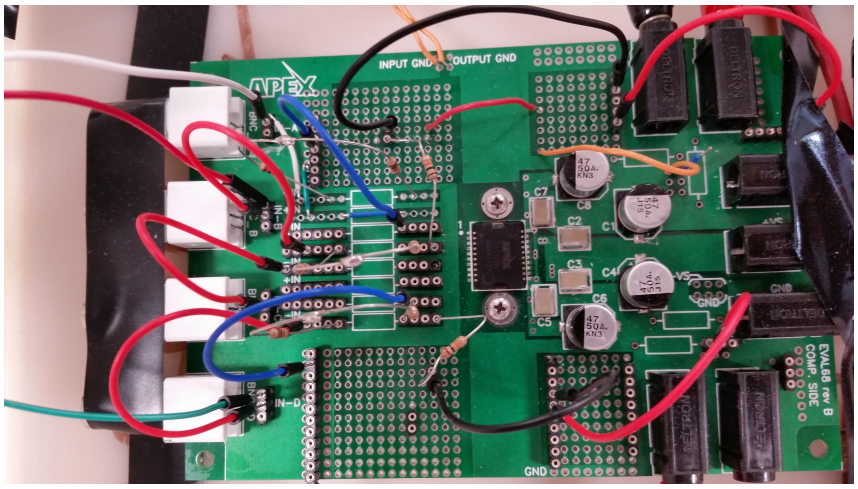

Figure 3.5: Image of the APEX EVAL68 rev. B power amplifier used to boost the current in the transmitter.

3.1.4 Receiver Amplifiers

The readings of the voltage across the load resistance in the receiver is very small. Thus a series of operational amplifiers are used to increase to voltage in order to measure the signal from the receiver coil.

The first operational amplifier is a LT1167 low-noise amplifier with a external resistor R_g of 60 or 120 Ohms, depending on the amount of gain needed. The formula for the gain is given in the data sheet [20]; however it is more accurate to measure the gain directly across the whole chain as will be discuss later.

The second and third (not used) operational amplifiers are LM741 amplifiers configure as inverting amplifiers with an expected gain of 50 each.

The actual gain of the complete amplification chain is measured and recorded in table 3.6 where the low-noise amplifier has an R_g of either 60 or 120 Ohms. For $R_g =$ 120 Ohm, the gains are consistently around 72 dB when the frequency is no less than 25 kHz, but depends linearly to 60 dB at 120 kHz. When $R_g = 60$ Ohm, the gain started at 74 dB for 1 kHz and rose to 105 dB at 15 kHz, but then dropped to 63 dB at 120 kHz.

3.1.5 Oscilloscope

Figure 3.6 shows the Agilent Technologies InfiniVision DSO-X 3034A digital oscilloscope used to get the sinewaves across the whole system. The green signal is the voltage across the transmitter resistance R_{TX} which is used to measure the current in the transmitter. The blue signal is the voltage output of the receiver coil with the gains from the both the low-noise amplifier and the inverting amplifier. All data is recorded on a USB stick in a CSV (i.e. comma separated) file that can be opened with any spreadsheet software.

3.1.6 Summary

A summary of the order of operation is given in figure 3.7. The circuits are represented in figures 2.13 and 2.17. The signal generator sends a sinewave of a fixed frequency to a power amplifier which powers the transmitter circuit and coil. Power is sent from the transmitter to the receiver by mutual induction. The induced voltage is amplified with a low-noise amplifier followed by an inverting amplifier.

Frequency (kHz)	Gain for $R_g = 120\Omega$ (dB)	Gain for $R_g = 60\Omega$ (dB)
1	73.0	74.2
2	73.2	76.5
3	73.4	78.8
4	73.5	80.9
5	73.5	82.8
6	73.5	84.7
7	73.5	86.4
8	73.4	88.1
9	73.4	89.8
10	73.3	91.5
15	73.0	105
20	72.8	96.6
25	72.3	90.5
30	71.8	86.6
40	70.5	81.9
50	69.5	78.3
60	68.4	75.3
70	67.1	72.8
80	65.8	70.5
90	64.5	68.4
100	63.2	66.6
110	61.8	64.9
120	60.5	63.6

Table 3.6: Table of the measured gains in the chain of receiver amplifiers.

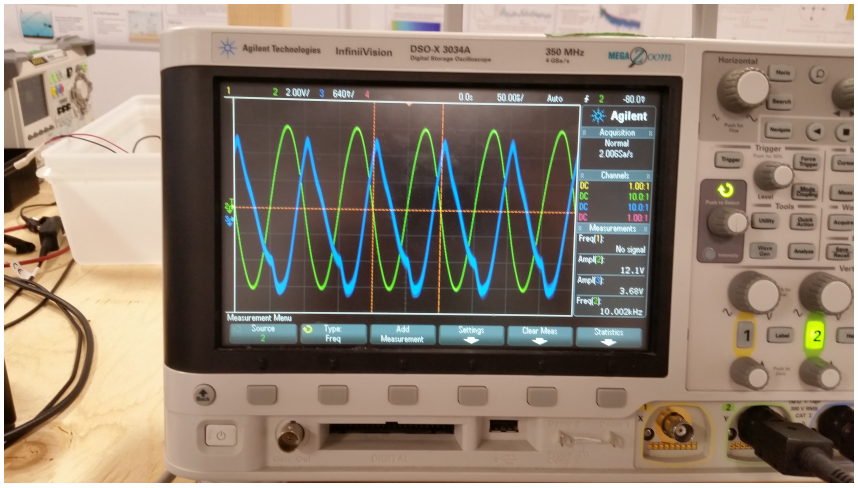

Figure 3.6: Image of the Agilent Technologies InfiniVision DSO-X 3034A digital oscilloscope used to record the signals. The green signal comes from resistor R_{TX} and the blue signal comes from the receiver after the chain of operational amplifiers

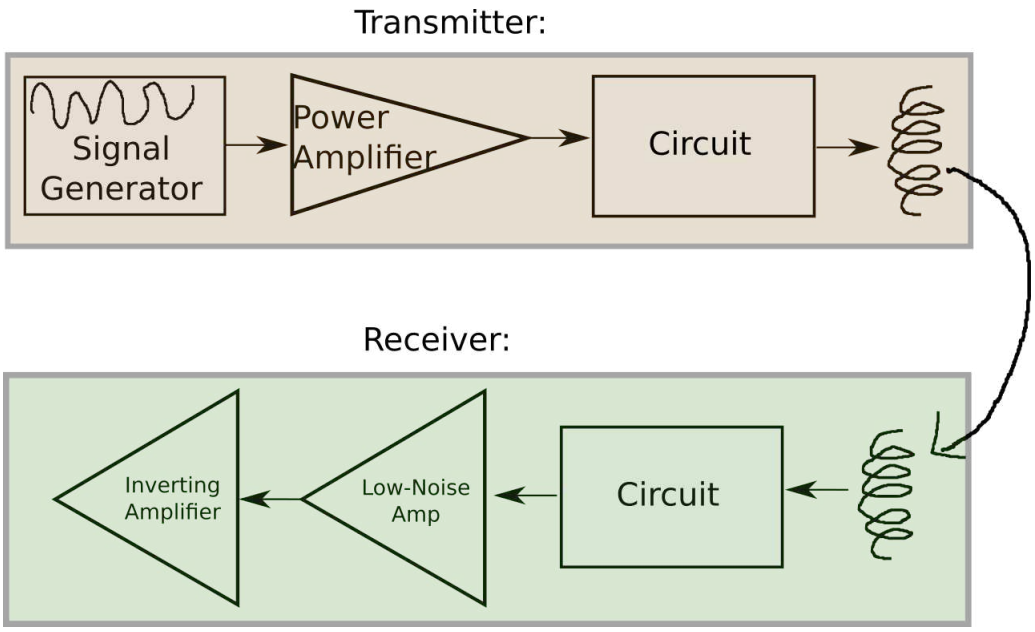

Figure 3.7: Schematic of the equipment.

3.2 Air Tests in the Lab

To ensure that the system works as expected, two experiments are performed in air at the UWStream lab. A wooden cart shown in figure 3.8 is made to easily move the receiver at a given distance from the transmitter. Wood is chosen for the cart instead of metal to minimize the risk that conducting material may affect the measurements. The receiver is tied to a vertical piece of wood screwed on the edge of the cart. The transmitter coil and all of the equipment are fixed on a table and placed as far away from both coils as possible. The circuit in the receiver is also placed on the table.

The experiments in the lab comprise of two tests. In test 1 (subsection 3.2.1), the mutual induction is measured for various coil distances and then compared with the models. In test 2 (subsection 3.2.2), the distance is fixed and a capacitor is added to verify the claim that a capacitor in the load improves the received signal.

3.2.1 Test1 - Verify Mutual Inductance Formula

The objective of this experiment is to verify the mutual inductance from formula (2.66) where the system is in the near field, but when the coils can be close together.

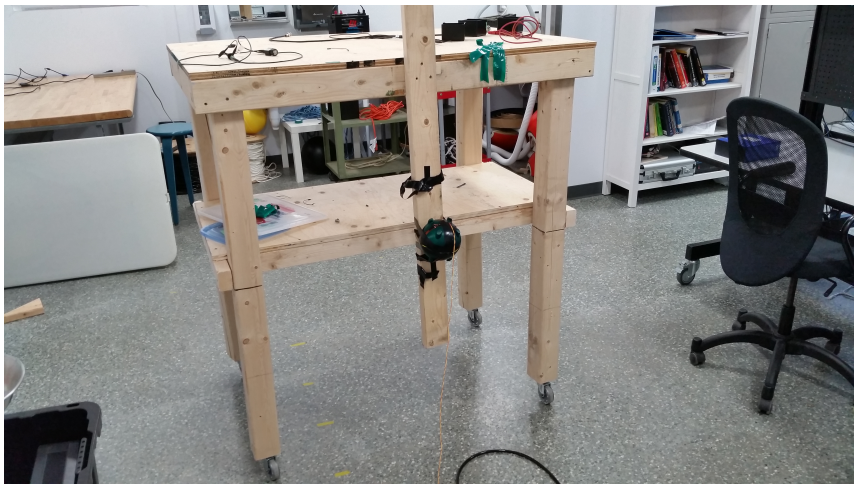

Figure 3.8: Image of the wooden cart used to perform air tests.

To do so, one measures the mutual inductance M for multiple coil distances d up to 4 meters and plots it against the expected curve from equation (2.68a).

Since the coil radius $\alpha_{TX} = \alpha_{RX} = \alpha = 6.5$ cm and the turn ratios $N_{TX} = N_{RX} = N = 35$ are the same for this and subsequent experiments, the formula from (2.66) will be rewritten as follows:

$$M = \bar{M}_0 \mathscr{I}\left(\frac{\alpha}{d}\right) \tag{3.1a}$$

$$\bar{M}_0 = \pi \mu_0 N^2 \alpha \tag{3.1b}$$

$$\mathscr{I}(x) = x \int_0^\infty J_1^2(xt) \mathrm{e}^{-t} \mathrm{d}t \tag{3.1c}$$

Note that when $\alpha \ll d$ (or $x \ll 1$), $\mathscr{I}(x) \approx x^3/2$ and hence M becomes the near-field dipole approximation from equation (2.67). Since $\alpha = 6.5$ cm, it is expected that M is inversely proportional to d^3 when $d \gg 20$ cm.

To measure the mutual inductance at a fixed distance, the transmitter is powered with a sinewave current of a given frequency and the voltage across the transmitter resistor R_{TX} and in the receiver are measured. This is repeated for multiple other frequencies between 1 and 25 kHz spread out in a logarithmic scale. This gives a profile of the voltage ratio $\mathscr{V}$ as a function of f similar to equation (2.82). A least-squares fit using equation (2.82) is applied to calculate the constant term A, which then can be used to obtain the mutual inductance M. The load resistance R_{RX} in this series

Name	Symbol	Value
Distances	d	Between 0.16 m and 4 m
Frequencies of Operation	f	1 kHz to 25 kHz
Transmitter Radius	α_{TX}	6.5 ± 0.5 cm
Receiver Radius	α_{RX}	6.5 ± 0.5 cm
Number of Turns in Transmitter	N_{TX}	35 ± 6
Number of Turns in Receiver	N_{RX}	35 ± 6
Transmitter Resistance	R_{TX}	5 Ω
Receiver Resistance	R_{TX}	10 Ω
Transmitter Impedance from Self-Inductance	$Z_{L_{TX}}$	See Table 3.1
Receiver Impedance from Self-Inductance	$Z_{L_{RX}}$	See Table 3.4
Mutual Inductance	M	Equation (3.1a)

Table 3.7: Summary of the parameters used in the mutual inductance measurements in the air.

of tests is chosen to be 10Ω to ensure that $f_l = 7.4$ kHz, which is within the range of frequencies and thus the profile will look like figure 2.16.

Once a series of values of M are obtained for various distances d, the dataset is plotted and compared with equation (3.1a). Another least-squares fit can be preformed to get $\bar{M}_0$ which can be compared to the expected value in (3.1b).

Table 3.7 summarises the parameters used for the the first test.

3.2.2 Test2 - Capacitor Performance

This experiment tests the premise in section 2.6.3 that a capacitor C_{RX} added to the receiver in parallel increases the voltage ratio near the resonance frequency given by $f_0 = 1/2\pi\sqrt{L_{RX}C_{RX}}$. The capacitor chosen is the 15 μF given in table 3.5 which allows the receiver to resonate at 8 kHz.

The distance is fixed to be 1 meter. Two sets of voltage measurements are taken as a function of frequency. The first set has the capacitor added and the second set will not. For the set with no capacitor, the dataset is compared with equation (2.82). However since the load resistance is now $R_{RX} = 240$ Ω, the cutoff frequency f_l is less than the frequencies of operation and thus $\mathscr{V} \approx Af$. For the case of the capacitor added, equation (2.85) is used.

Table 3.8 summarises the parameters used for the the second test.

Name	Symbol	Value
Distances	d	1 m
Frequencies of Operation	f	1 kHz to 25 kHz
Resonance Frequency	f_0	8 kHz
Transmitter Radius	α_{TX}	6.5 ± 0.5 cm
Receiver Radius	α_{RX}	6.5 ± 0.5 cm
Number of Turns in Transmitter	N_{TX}	35 ± 6
Number of Turns in Receiver	N_{RX}	35 ± 6
Transmitter Resistance	R_{TX}	5 Ω
Receiver Resistance	R_{TX}	240 Ω
Transmitter Impedance from Self-Inductance	$Z_{L_{TX}}$	See Table 3.1
Receiver Impedance from Self-Inductance	$Z_{L_{RX}}$	See Table 3.4
Impedance from Capacitance	Z_C	See Tables 3.5
Mutual Inductance	M	Equation (3.1a)

Table 3.8: Summary of the parameters used in the voltage ratio measurements with a capacitor.

3.3 Air-Water Tests in the Dalhousie Aquatron

This test is performed at the Dalhousie Aquatron on May 2021. Its objectives are to confirm that a signal can be received from a coil underwater, and verify that the mutual inductance agrees with the theory (equation (3.1a)). Figure 3.9 shows a diagram of the setup on the water. Figure 3.10 shows a photo taken of the setup.

The tanks of water contain a pontoon that was used to move the system away from the walls to minimize the effects from boundaries. The system consists of two wooden sticks tied to the pontoon with rope. The use of any metal are kept to a minimum to avoid magnetic noise in the system. The sticks are placed next to each other. One is anchored next to the pontoon and can not be moved, while the other can be moved vertically to change the distance between the transmitter and receiver. In this test, the transmitter is lowered 1 meter. The receiver is placed on the fixed stick 1 m above the water surface. The transmitter is placed at the bottom of the movable stick. To keep the transmitter level, a weight is tied onto the transmitter as

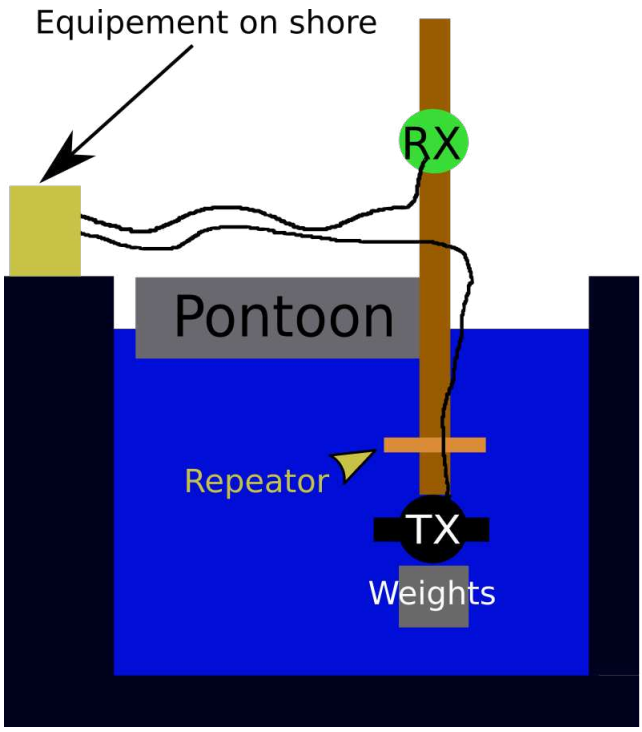

Figure 3.9: Diagram of the Aquatron test setup.

Figure 3.10: Photograph of the Aquatron test setup.

shown in figure 3.11.

Figure 3.11: Closer look at the underwater transmitter with a weight tied onto.

The electrical equipment is placed on the shore, and connected by wire to both the transmitter and receiver as seen in figure 3.12. The same schematic from figure 3.7 applies here.

Table 3.9 summarises the parameters used for the measurements in the Aquatron. Since the frequencies of operation are below 25 kHz for the test, the system is in the near-field and thus the conductivity of water has no effect. Equation (3.1a) is used to estimate the mutual inductance. Distances are fixed and a capacitor is used to resonate at 8 kHz.

As in the air experiments, a series of voltage measurements in the receiver (with gains) and the fixed transmitter resistance R_{TX} are recorded for a given frequency between 1 and 25 kHz. The resulting voltage ratio plot vs frequency should resemble equation (2.85). A least-squares fit is used to determine the mutual inductance and then compared with equation (3.1a).

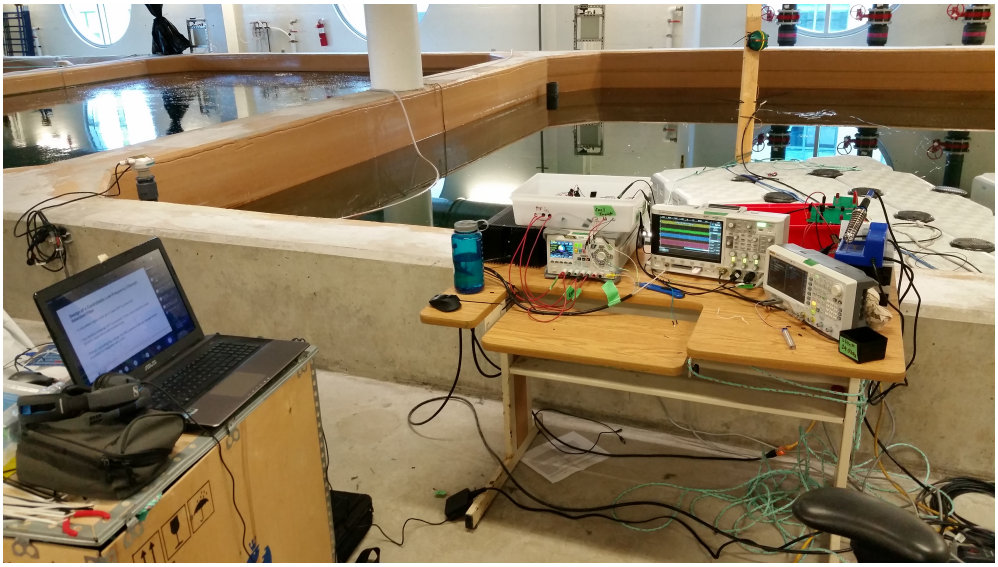

Figure 3.12: Image of the equipment used to power the transmitter and measure the receiver.

Name	Symbol	Value
Transmitter depth below the boundary	d	1.0 ± 0.1 m
Receiver height above water	h	1.0 ± 0.1 m
Resonant Frequency	f_0	8 kHz
Frequencies of Operation	f	1 kHz to 25 kHz
Transmitter Radius	α_{TX}	6.5 ± 0.5 cm
Receiver Radius	α_{RX}	6.5 ± 0.5 cm
Number of Turns in Transmitter	N_{TX}	35 ± 6
Number of Turns in Receiver	N_{RX}	35 ± 6
Transmitter Resistance	R_{TX}	5Ω
Receiver Resistance	R_{TX}	240Ω
Transmitter Impedance from Self-Inductance	$Z_{L_{TX}}$	See Table 3.1
Receiver Impedance from Self-Inductance	$Z_{L_{RX}}$	See Table 3.4
Impedance from Capacitance	Z_C	See Table 3.5
Mutual Inductance	M	Equation (3.1a)

Table 3.9: Summary of the parameters used in the Dalhousie Aquatron measurements.

Chapter 4

Results and Discussion

In this chapter, an analysis of the data for both air and Aquatron trials is performed and the results are discussed. Section 4.1 details how the collected sinewave measurements are processed to obtain voltage ratios, which are used to perform least-square fits to find the mutual inductance. The section 4.2 presents and discusses the data obtained from the first experiment in the air (subsection 3.2.1) where the mutual inductance is measured versus distance. Section 4.3 discusses the results for the second test (subsection 3.2.2) where a capacitor is added. Finally section 4.4 goes over the findings from the Aquatron experiment.

4.1 Data Analysis

This section presents how the data collected from an oscilloscope is used and the mutual induction tests are processed to obtain a series of plots of voltage ratios vs frequency. These plots are then fitted to equations (2.82) and (2.85) to measure the mutual induction.

The oscilloscope records two voltages of the system as a function of time and outputs as a CSV file. The name of the file is of the format "f_XXXpXkHz.csv" where the X's are replaced with the frequency in kilohertz of the AC signal sent by the signal generator to the system (the "p" represents the decimal point). These files are grouped in a series of directories named via the test name followed by the parameters used (i.e. distance value or if a capacitor is used). Figure 4.1 shows visually how the data is stored.

In each CSV file there are three columns of data. Figure 4.2 is an example of how each CSV file is structured. The first column is the time at which the oscilloscope took a voltage measurement. The second column is the voltage across the fixed

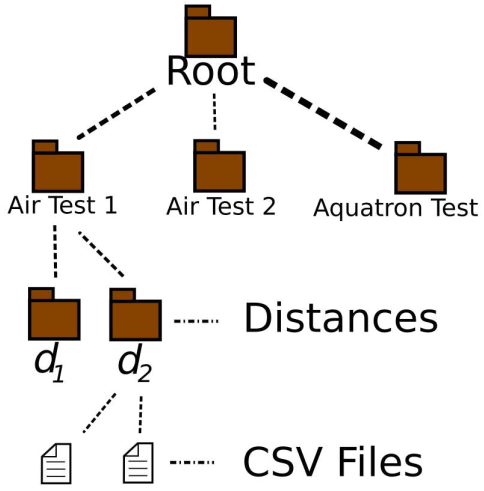

Figure 4.1: Image representation of the directory structure used to store the measured voltages.

resistor R_{TX}. The last column is the measured voltage in the receiver after passing through the two amplifiers. The peak-to-peak voltage for each of the voltage columns is evaluated in order to make voltage ratio plots. This is done by passing each CSV into a Python code that does basic signal process on the columns.

Figure 4.3 illustrates how the code takes the waves and gets a peak-to-peak voltage. The signal is first passed through a Butterworth bandpass filter to remove any noise. Such a filter needs a upper and lower cutoff frequency. The script can get the frequency of operation directly from the CSV filename and then take $\pm 1\%$ of that value for the cutoffs. This leaves a clean wave, but with artifacts at the start time values and thus the code only takes the latter part of the filtered signal. A least-squares sine function fit of the form $V(t) = A\sin(Bt + C) + D$ is applied to the filtered signal with A, B, C, and D the constants to be calculated. The relevant constant needed is A which is the half of the peak-to-peak voltage. 4.4 shows a sample process of the filtering and curve-fitting. Once each peak-to-peak voltage is found, it returns the ratio of the two.

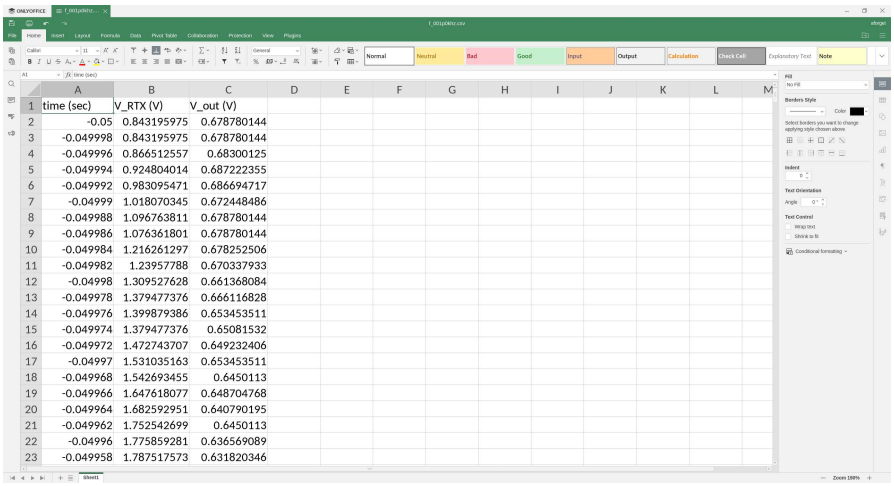

	A	B	C
1	time (sec)	V_RTX (V)	V_out (V)
2	-0.05	0.843195975	0.678780144
3	-0.049998	0.843195975	0.678780144
4	-0.049996	0.866512557	0.68300125
5	-0.049994	0.924804014	0.687222355
6	-0.049992	0.983095471	0.686694717
7	-0.04999	1.018070345	0.672448486
8	-0.049988	1.096763811	0.678780144
9	-0.049986	1.076361801	0.678780144
10	-0.049984	1.216261297	0.678252506
11	-0.049982	1.23957788	0.670337933
12	-0.04998	1.309527628	0.661368084
13	-0.049978	1.379477376	0.666116828
14	-0.049976	1.399879386	0.653453511
15	-0.049974	1.379477376	0.65081532
16	-0.049972	1.472743707	0.649232406
17	-0.04997	1.531035163	0.653453511
18	-0.049968	1.542693455	0.6450113
19	-0.049966	1.647618077	0.648704768
20	-0.049964	1.682592951	0.640790195
21	-0.049962	1.752542699	0.6450113
22	-0.04996	1.775859281	0.636569089
23	-0.049958	1.787517573	0.631820346

Figure 4.2: Sample view of a CSV file containing the measured voltages from the oscilloscope.

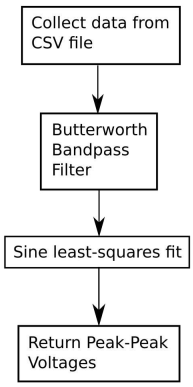

Figure 4.3: Flowchart of the process of taking the voltages measured from a CSV file to a peak-to-peak voltage.

4.2 Results of Air Test 1 - Mutual Induction vs Distance

In this section, the results of experiment 1 from subsection 3.2.1 are presented, followed by a discussion of the findings.

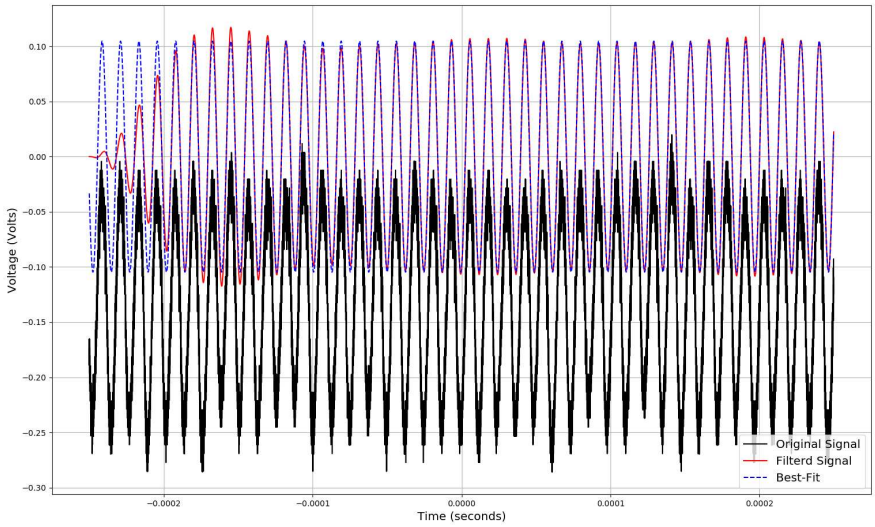

Figure 4.4: Sample image of the analysis of the measured signals. A bandpass filter is used followed by a best-fit sinewave.

4.2.1 Results

To proceed, the steps are to first fix a distance d and measure the voltages to obtain the voltage ratio as a function of frequency. This is then repeated for multiple distances. As demonstration, the following shows the plot for the voltage ratio at $d = 1$ m.

Table 4.1 shows a sample dataset for the voltage ratios measured for a coil separation of 1 m. Figure 4.5 shows the resulting plot along with the best-fit curve using equation 2.82. Using the data from table 3.7, the expected cutoff frequency is $f_l = 7.4$ kHz. The best-fit gives $f_l = 7.3 \pm 0.1$ kHz, which is within the expected value. The best-fit value for the constant A from equation (2.83) is $A = (2.2 \pm 0.1) \times 10^{-5}$ ms, which gives rise to a mutual inductance of $M = 29 \pm 4$ nH.

After repeating for multiple distances, the measured mutual inductances are presented in table 4.2 and the plot is shown in figure 4.6. The theoretical value for the mutual induction given by equation (3.1a) is also shown in the plot.

Frequency (kHz)	Voltage Ratio (dB)
1.0	-93.6
1.3	-91.1
1.6	-89.5
2.0	-87.6
2.5	-85.8
3.2	-83.9
4.0	-82.3
6.3	-79.6
7.9	-78.6
10	-77.7
13	-77.1
16	-76.8
20	-76.1
25	-76.6

Table 4.1: Sample voltage ratio data obtained for a mutual induction system with the coils 1 m apart.

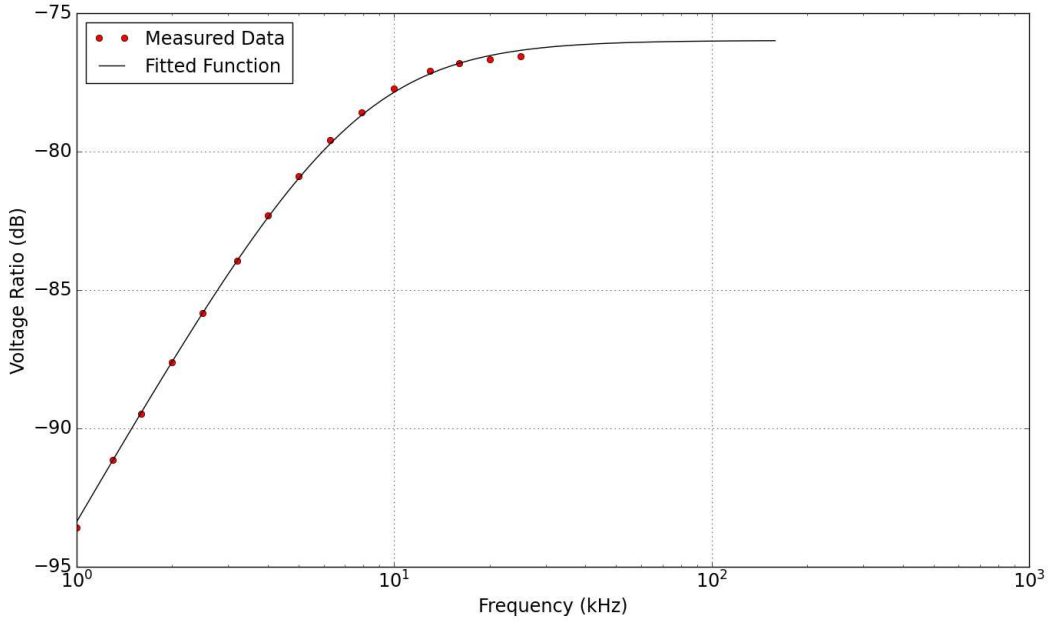

Figure 4.5: Sample plot of the voltage ratio vs frequency obtained from the mutual induction system with coils separated 1 m apart.

Distance (m)	Mutual Inductance (nH)
0.16 ± 0.01	4200 ± 600
0.20 ± 0.01	2600 ± 400
0.25 ± 0.01	1500 ± 200
0.32 ± 0.02	830 ± 100
0.40 ± 0.02	390 ± 60
0.50 ± 0.02	220 ± 30
0.63 ± 0.03	110 ± 20
0.79 ± 0.04	57 ± 7
1.00 ± 0.05	29 ± 4
1.30 ± 0.06	13 ± 2
1.60 ± 0.07	6.3 ± 1
2.00 ± 0.08	6.3 ± 1
2.50 ± 0.09	4.5 ± 0.7
3.20 ± 0.10	2.8 ± 0.4
4.00 ± 0.12	2.2 ± 0.3

Table 4.2: Table with the measured mutual inductances as a function of distance.

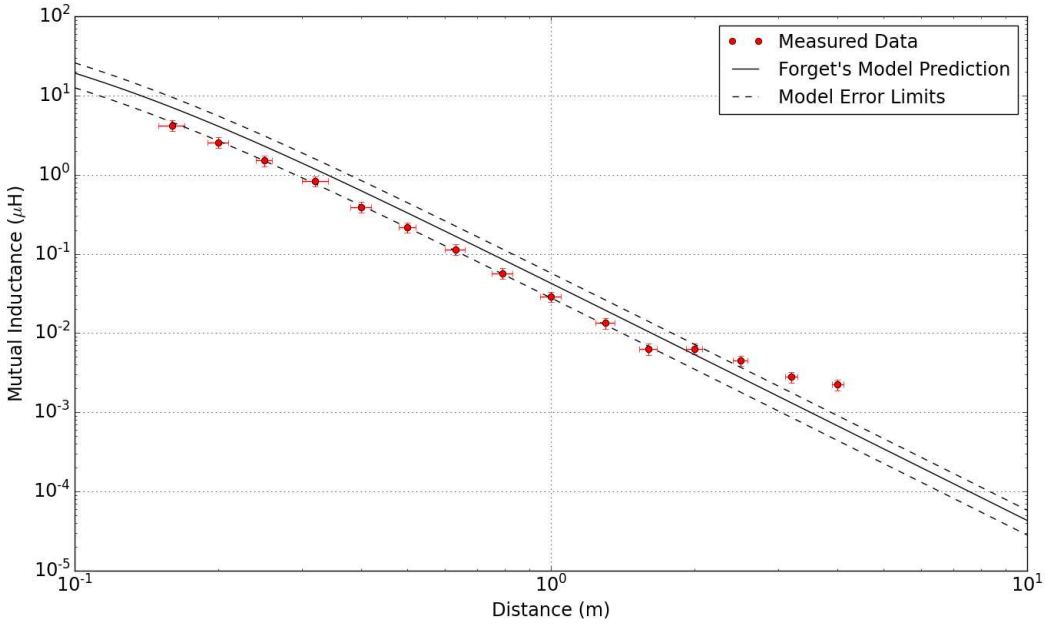

Figure 4.6: Plot of the measured mutual inductance as a function of distance in the first experiment (subsection 3.2.1) along with the expected curve given by equation (3.1a).

4.2.2 Discussion

First note that for the voltage ratio plot for $d = 1$ m as shown in figure 4.5, the profile behaves like a high-pass filter with cutoff frequency of 7.4 kHz. This is the expected result and is consistent with all of the other distances.

Figure 4.6 shows that the mutual inductance follows the correct trend that the theory (equation (3.1a)) predicts for distances up to 1.6 m. The relationship of M being proportional to $1/d^3$ is seen in the data between 0.32 and 1.6 meters. Thus for coils of $\alpha = 6.5$ cm, it is reasonable to use equation (2.67) or (2.70) depending on how far away the coils are, or if the frequency is large enough. The model does overestimate the measured values below 1.6 m, but is still within the expected error range. The primary cause of error for the model is from the number of turns N of the coils. Since in this experiment M is proportional to N^2, a miscount of the number of turns can cause significant errors in the mutual induction.

At distances of 2 m or above, the measured M is significantly over what the model predicts. The reason for this is clear when investigating the measured voltages at these distances. Figure 4.7 shows a sample voltage reading from the receiver for $d = 4$ m and $f = 10$ kHz. The noise floor distorts the signal too much for a filter to recover the signal properly. This suggests that at distances larger than 2 m, one should perform the mutual induction tests in a more open area where there are fewer electrical disturbances than presents is in the lab. Therefore, due to the limitations in the testing environment, the results for $d \geq 2$ m are inconclusive.

4.3 Results of Air Test 2 - Capacitor in the Receiver

In this section, the results of the test 2 from subsection 3.2.2 is presented and discussed where the distance between the coils are fixed at 1 meter. Instead of measuring M, this test verifies the claim in equation (2.85) that adding a capacitor C_{RX} in parallel to the load resistance R_{RX} improves the reading in the oscilloscope near the resonance frequency of $f_0 = 1/2\pi\sqrt{L_{RX}C_{RX}}$.

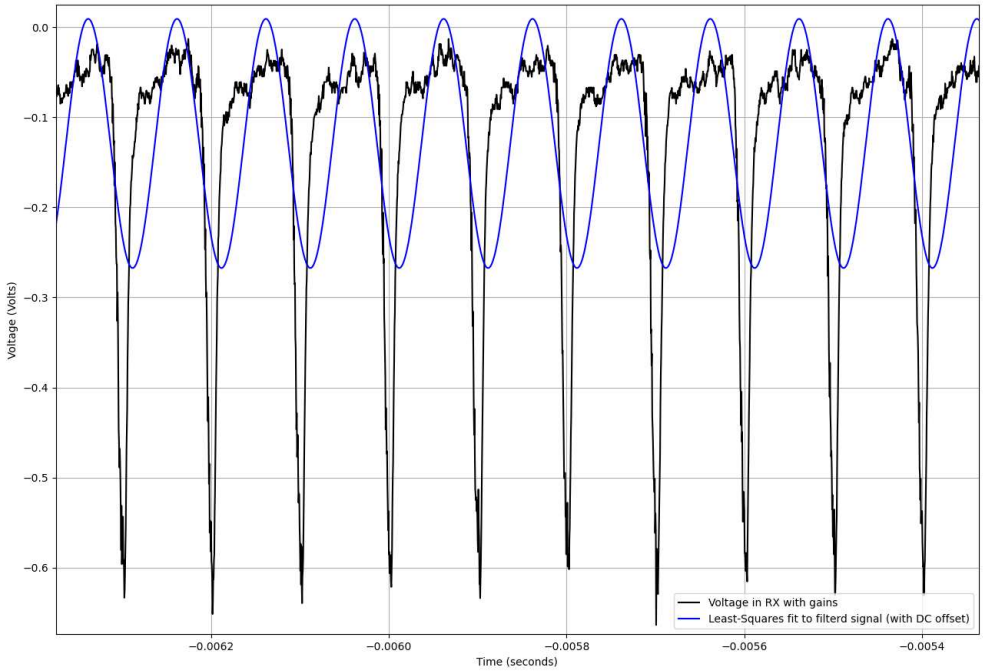

Figure 4.7: Plot of the measured voltage across the receiver (with gains) at $d = 4$ m and $f = 10$ kHz along with the least-square fit to the filtered sinewave.

4.3.1 Results

Note that unlike in the first test, the load resistance is now $R_{RX} = 240\ \Omega$. This means that when there is no capacitor, the cutoff frequency f_l from (2.82) is 80 kHz. This is beyond the 25 kHz limit in the testing equipment and thus equation (2.82) can be approximated as:

$$\mathscr{V}(f) = Af \tag{4.1}$$

Therefore in a log-decibell plot, the voltage ratio will look like a straight line with slope of 1.

Figure 4.8 shows the measured voltage ratios as a function of frequency along with the fitted curve from equation (4.1). The constant is $A = 3.5 \pm 0.1$ milliseconds.

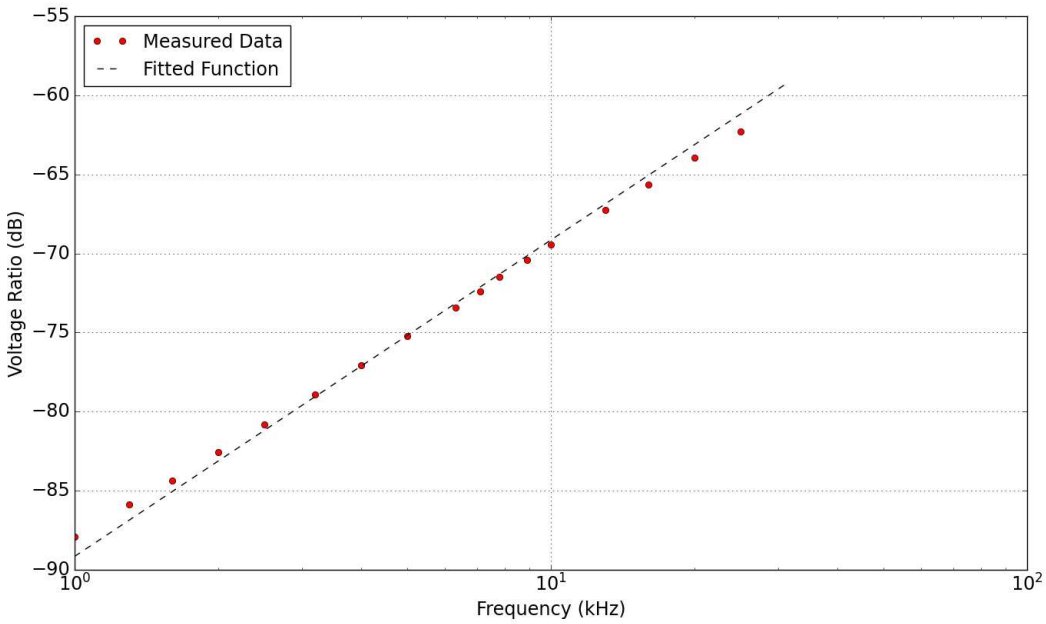

Figure 4.8: Plot of the voltage ratio in test 2 (subsection 3.2.2) with no capacitor along with the best-fit function from equation (4.1).

For the case with a capacitor, Figure 4.9 shows the measured voltage ratios as a function of frequency along with the fitted curve from equation (2.85). The constant is $A = 3.0 \pm 0.2$ milliseconds, which is very close to the same value in the no capacitor

scenario. Using the formulas, the predicted resonance frequency and cutoff frequencies are $f_0 = 7.2$ kHz and $f_l = 15$ kHz. The best-fit gives $f_0 = 6.8 \pm 0.2$ kHz and $f_l = 15 \pm 2$ kHz, which matches the theoretical predictions within the error tolerances.

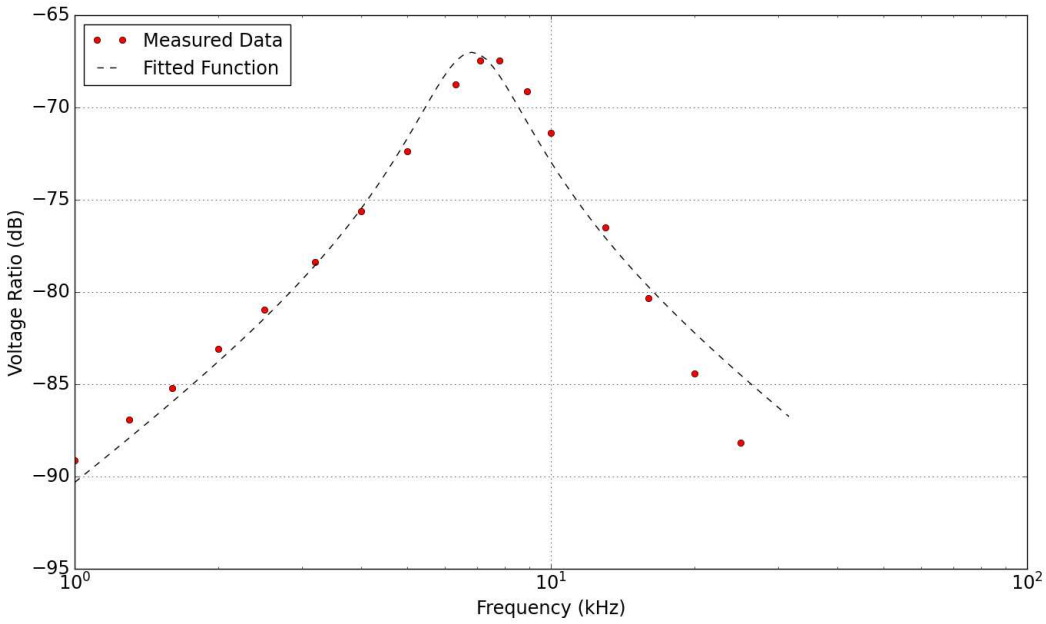

Figure 4.9: Plot of the voltage ratio in test 2 (subsection 3.2.2) with a capacitor along with the best-fit function from equation (2.85).

Finally, the two plots are compared. Figure 4.10 is the result of dividing the data from figure 4.9 by figure 4.8. This plot determines if the capacitor has an improvement on the measured voltage ratio.

4.3.2 Discussion

As figure 4.10 demonstrates, the capacitor does improve the voltage ratio near the resonance frequency by about 6 dB. At frequencies $f \ll f_0$ and f_l, the curve levels off. This is to be expected when comparing equations (2.82) with (2.85). In both cases, $\mathscr{V}$ is proportional to f and thus should cancel when taking their ratios. At large frequencies $f \gg f_0$ and f_l, $\mathscr{V}_{\text{noCaps}}$ is a constant, but $\mathscr{V}_{\text{Caps}}$ is proportional to $1/f$ hence the drop-off shown in figure 4.10 beyond the resonance frequency.

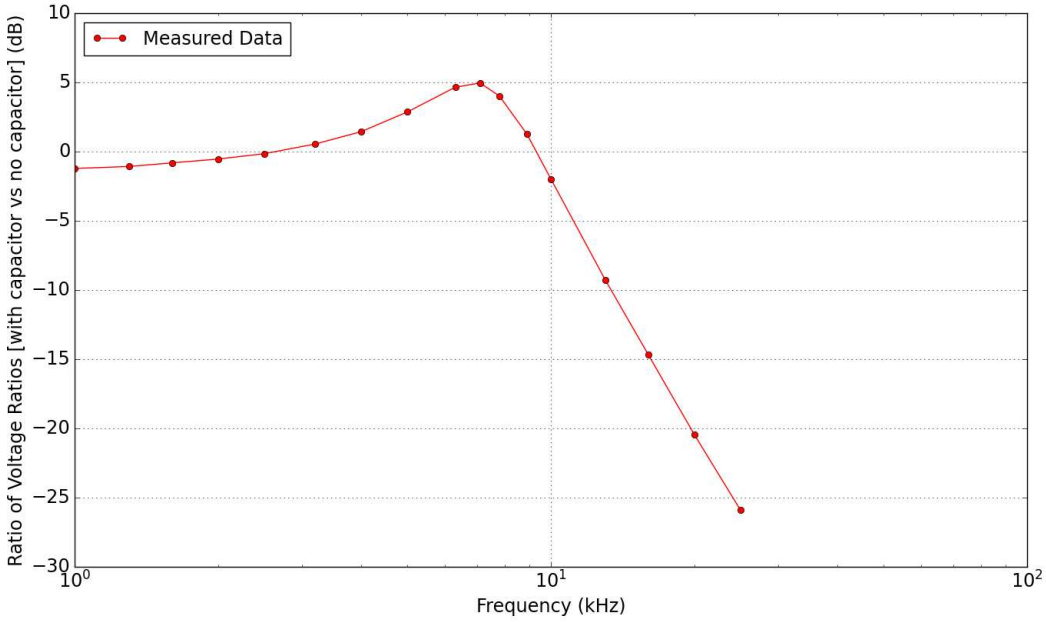

Figure 4.10: Plot of the ratio of figure 4.9 to figure 4.8.

The curve stays within 1 dB from the maximum within 500 Hz from the peak. Decreasing R_{RX} would increase the peak at the expense of a shorter bandwidth. The choice of 240 Ω seems to be a reasonable one.

4.4 Aquatron Results

In this section, the voltage ratio obtained from the Aquatron is presented and discussed. It is noted that the same capacitor as in the lab test 2 is used, and that the case of $R_g = 120$ Ω is used in the low-noise amplifier.

Figure 4.11 gives the resulting measured voltage ratios of the test in the Aquatron along with the theoretical prediction using equation (3.1a) to calculate M and (2.85) to get the curve. Tow fitted functions are shown; the dashed black curve uses all of the data points, whereas the dashed blue curve excludes the last two points which appears questionable.

The expected curve is only about 2 dB over the measured data, which corresponds

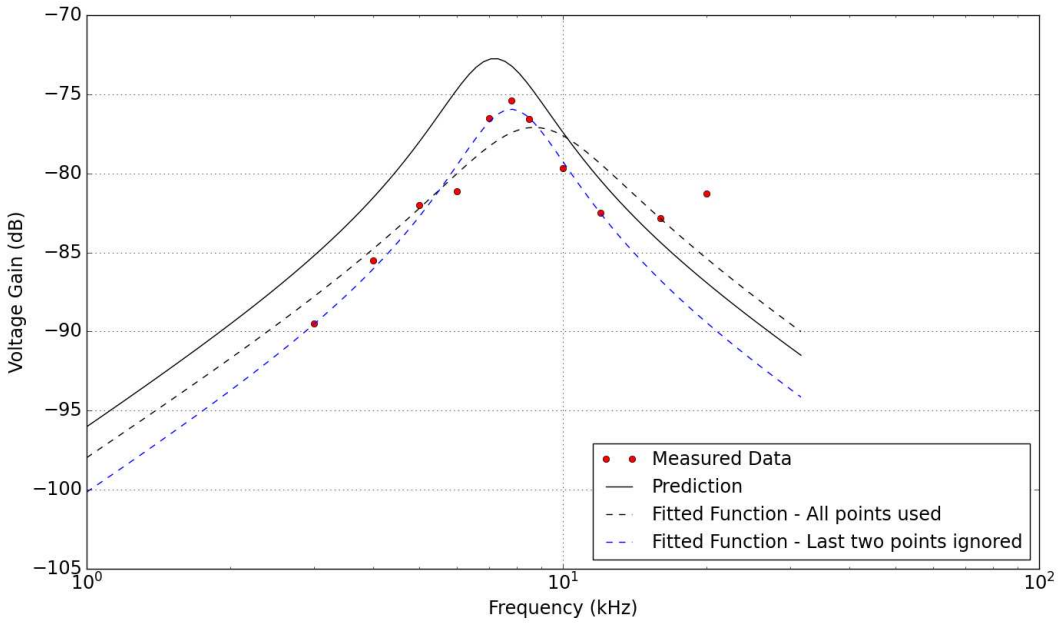

Figure 4.11: Plot of the measured voltage ratio obtained from the Aquatron along with two best-fit functions and the predicted result.

to a mutual inductance of $M = 13$ nH. Using the fitted functions, $M = 10 \pm 2$ nH for the fit with all points and $M = 8 \pm 1$ nH for the better fit with the last two points removed. This suggest that the model from equation (3.1a) is accurate for a air-water coil system with the transmitter underwater at a single depth value of 1.5 m. More depths are needed to conclusively show that the model works. However, the results thus far are promising, and merit further exploration.

For the other parameters, the cutoff frequencies f_l are 11 ± 1 kHz for the 'bad' fit and 16 ± 2 kHz for the 'good' fit. The predicted value is 15 kHz and thus the good fit is closer. The resonance frequencies f_0 are 8.7 ± 0.6 kHz for the 'bad' fit and 7.8 ± 0.2 kHz for the 'good' fit. The theory predicts 7.2 kHz, which is close to the result from the 'good' fit.

Chapter 5

Conclusion

5.1 Conclusion

This thesis explores a new mathematical model for the determination of mutual inductance in communication systems deployed in an air-water context. The proposed model provides more accuracy than other models based on numerical simulations and comparisons with known approximate models in extreme frequencies and/or distances. The new model is also faster to compute than simulating the fields directly from Maxwell's equations as it only requires evaluating a single integral as opposed to numerically solving a system of partial differential equations. Under given conditions, the general model derived can be approximated to simpler known equations. The experimental results verify the model at the near-field for air context and suggest it works as well in water. Experimental verification for the far-field in an air-water context is not accomplished due to the restrictions for distances and frequencies in the testing environment.

The model also gives the best frequencies to operate at a given TX depth. As shown in subsection 2.5.4, the optimal frequency for maximum induced voltage at a fixed transmitter current gets smaller very quickly which makes MI communication more difficult at greater distances. The maximum itself also gets significantly smaller with increasing coil separation. Referring to figure 2.11, for 100 m, the best frequency is approximately 50 Hz, which significantly limits the channel capacity. Improvements to this simple coil antenna model must be proposed to allow a higher frequency of operation at distances greater than 50 m.

On a related note, this thesis uses the proposed model to investigate the possibility of adding a passive repeater coil to improve performance. Such a coil is placed in between the transmitter and receiver and the best location and size are determined

and compared with no repeater. The finding of this thesis indicates that adding a single passive repeater is not a good method for improving the performance of signal transmission. The analysis indicates that the repeater must be 10 times the size of the other coils, or must be close to the other coils.

5.2 Future Work

The results of this inquiry are promising and support additional research in four areas. First an error and noise analysis to mitigate potential sources of error in a MI system. Second, conduct an ocean trial to overcome the limitations present at the Dalhousie Aquatron. Additionally, other signals and coil configurations should be explored.

The error analysis should consider three factors. First, coil misalignment should be examined. [21] has already made extensive analysis for coils in air. This research should be extended to a study of coil misalignment in an air-water context. Second, the noise present in the equipment used in MI communication should be quantified in order to develop mitigation strategies. Third, an extensive analysis of external magnetic interference should be conducted. Potential sources to investigate include the earth, ships, water current, marine life and sea floor.

An ocean trial would enable testing the proposed MI model at greater distances than provided in the Aquatron. A depth of 20 meters is more useful to real world deployment of MI communication systems. An ocean environment will allow one to determine the maximum distance or frequency beyond which the attenuation due to conductivity takes place.

Once a successful error analysis is completed and sea trails of MI are conducted, research into employing other signals can follow. In particular, digital signals such as phase-shift keying would be useful to investigate. This would include a study on the channel capacity of the MI communication system.

Finally, there are other possible coil configurations to consider. Examples include, the use of multiple active transmitters in an array, and the use of a multiple-input

multiple output (MIMO) setup. While the use of a repeater was not found to be useful, the use of metal surfaces near the transmitter to improve the system performance could be explored.

Appendix A

Vector Calculus Review

A *scalar field* is a function that takes a spatial position (x, y, z) and possibly time t and returns a real number. The charge density $\rho(x, y, z, t)$ of an object is an example of a physical quantity that can be modeled as a scalar field. By contrast, a *vector field* is a rule that accepts a coordinate (x, y, z) and possibly time t and returns a vector at that coordinate. Electric $\mathbf{E}(x, y, z, t)$ and magnetic $\mathbf{H}(x, y, z, t)$ fields are examples of vector fields.

Vector fields obey the same operations as regular vectors (addition '+', scalar multiplication, negation '−', dot product '•', cross product '×') provided that the operation is done with matching coordinates (i.e. $\mathbf{V}(x, y, z, t) + \mathbf{U}(x, y, z, t)$ is ok, but $\mathbf{V}(x, y, z, t) + \mathbf{U}(x', y', z', t')$ is not).

Unit vector fields based on the Cartesian coordinates $\hat{\mathbf{x}}, \hat{\mathbf{y}}, \hat{\mathbf{z}}$ are defined to have unit length and are oriented towards the increasing value of the corresponding coordinate. An arbitrary vector field $\mathbf{V}(x, y, z, t)$ can be written as follows:

$$\mathbf{V}(x, y, z, t) = V_x(x, y, z, t)\hat{\mathbf{x}} + V_y(x, y, z, t)\hat{\mathbf{y}} + V_z(x, y, z, t)\hat{\mathbf{z}} \tag{A.1}$$

Here, V_x, V_y, V_z are scalar fields called the *components* of $\mathbf{V}$. They represent the contributions of $\mathbf{V}$ that are oriented in the corresponding coordinate. Similar unit vectors exist for cylindrical (s, ϕ, z) and spherical (r, ϕ, θ) coordinates. The position vector $\mathbf{r} = x\hat{\mathbf{x}} + y\hat{\mathbf{y}} + z\hat{\mathbf{z}}$ is defined to denote the point (x, y, z) as a vector field.

There are three major differentiation operations in vector calculus. All three can be represented in terms of the following operator:

$$\nabla = \hat{\mathbf{x}}\frac{\partial}{\partial x} + \hat{\mathbf{y}}\frac{\partial}{\partial y} + \hat{\mathbf{z}}\frac{\partial}{\partial z} \tag{A.2}$$

This is not a vector field, but can be treated as one to easily reconstruct the following three operations:

A.1 The gradient

The *gradient* of a scalar field $f(\mathbf{r})$ creates a vector field defined as:

$$grad(f)(\mathbf{r}) = \nabla f(\mathbf{r}) = \frac{\partial f(\mathbf{r})}{\partial x}\hat{\mathbf{x}} + \frac{\partial f(\mathbf{r})}{\partial y}\hat{\mathbf{y}} + \frac{\partial f(\mathbf{r})}{\partial z}\hat{\mathbf{z}} \tag{A.3}$$

At a point $\mathbf{r}$, the orientation of $\nabla f(\mathbf{r})$ gives direction of fastest rate of increase of $f(\mathbf{r})$ and the rate of change in that direction is $|\nabla f(\mathbf{r})|$. Possible minimum and maximum points of $f(\mathbf{r})$ are located where $\nabla f(\mathbf{r}) = 0$.

Equation A.3 gives the gradient in Cartesian components. In cylindrical components:

$$\nabla f(\mathbf{r}) = \frac{\partial f(\mathbf{r})}{\partial s}\hat{\mathbf{s}} + \frac{1}{s}\frac{\partial f(\mathbf{r})}{\partial \phi}\hat{\phi} + \frac{\partial f(\mathbf{r})}{\partial z}\hat{\mathbf{z}} \tag{A.4}$$

And in spherical components:

$$\nabla f(\mathbf{r}) = \frac{\partial f(\mathbf{r})}{\partial r}\hat{\mathbf{r}} + \frac{1}{r\sin\theta}\frac{\partial f(\mathbf{r})}{\partial \phi}\hat{\phi} + \frac{1}{s}\frac{\partial f(\mathbf{r})}{\partial \theta}\hat{\theta} \tag{A.5}$$

An arbitrary vector field $\mathbf{V}$ is called *irrotational* if there exist a scalar field $f(\mathbf{r})$ such that $\mathbf{V}(\mathbf{r}) = -\nabla f(\mathbf{r})$. Electric fields from static charges is an example of an irrotational field since the electric potential V is related by $\mathbf{E} = -\nabla V$. Section A.2 gives a condition on when a vector field is irrotational. All of the information of an irrotational field can be described by its corresponding scalar field.

A.2 The curl

The *curl* of a vector field $\mathbf{V}$ gives another vector field defined as:

$$\begin{aligned} curl(\mathbf{V})(\mathbf{r}) = \nabla \times \mathbf{V}(\mathbf{r}) = \left(\frac{\partial V_z(\mathbf{r})}{\partial y} - \frac{\partial V_y(\mathbf{r})}{\partial z}\right)\hat{\mathbf{x}} + \left(\frac{\partial V_x(\mathbf{r})}{\partial z} - \frac{\partial V_z(\mathbf{r})}{\partial x}\right)\hat{\mathbf{y}} \\ + \left(\frac{\partial V_y(\mathbf{r})}{\partial x} - \frac{\partial V_x(\mathbf{r})}{\partial x}\right)\hat{\mathbf{z}} \end{aligned} \tag{A.6}$$

Corresponding versions for cylindrical and spherical components can be found in [18].

$|\nabla \times \mathbf{V}(\mathbf{r})|$ gives how much $\mathbf{V}(\mathbf{r})$ 'circulates' around the point $\mathbf{r}$. The orientation of $\nabla \times \mathbf{V}(\mathbf{r})$ is given by the right-hand rule.

Points where $\nabla \times \mathbf{V}(\mathbf{r}) = 0$ are where there is no circulation. Note that, for a scalar field $f(\mathbf{r})$, it is always true that $\nabla \times \nabla f(\mathbf{r}) = 0$. Thus if $\nabla \times \mathbf{V}(\mathbf{r}) = 0$ everywhere, then $\mathbf{V}(\mathbf{r})$ is irrotational and thus there is a scalar field $f(\mathbf{r})$ such that $\mathbf{V}(\mathbf{r}) = -\nabla f(\mathbf{r})$.

A.3 The divergence

The *divergence* of a vector field $\mathbf{V}$ gives a scalar field defined as:

$$div(\mathbf{V})(\mathbf{r}) = \nabla \bullet \mathbf{V}(\mathbf{r}) = \frac{\partial V_x(\mathbf{r})}{\partial x} + \frac{\partial V_y(\mathbf{r})}{\partial y} + \frac{\partial V_z(\mathbf{r})}{\partial z} \tag{A.7}$$

Corresponding versions for cylindrical and spherical components can be found in [18].

$\nabla \bullet \mathbf{V}(\mathbf{r})$ gives the flux per unit area of $\mathbf{V}(\mathbf{r})$ across an infinitesimally small box centered at $\mathbf{r}$. If $\nabla \bullet \mathbf{V}(\mathbf{r}) > 0$, more vectors $\mathbf{V}$ diverge away from $\mathbf{r}$. If $\nabla \bullet \mathbf{V}(\mathbf{r}) < 0$, more vectors $\mathbf{V}$ converge towards $\mathbf{r}$. If $\nabla \bullet \mathbf{V}(\mathbf{r}) = 0$, the point $\mathbf{r}$ is not a sink nor a source for $\mathbf{V}(\mathbf{r})$.

Note that $\nabla \bullet (\nabla \times \mathbf{V}(\mathbf{r})) = 0$ for any vector $\mathbf{V}(\mathbf{r})$. Thus if $\nabla \bullet \mathbf{U}(\mathbf{r}) = 0$ for some vector $\mathbf{U}(\mathbf{r})$, then there is a vector $\mathbf{V}(\mathbf{r})$ such that $\mathbf{U}(\mathbf{r}) = \nabla \times \mathbf{V}(\mathbf{r})$.

A.4 The Laplacian

The *Laplacian* is a second-order differential operator that is defined in terms of the previous three operators. Is it defined for both a scalar field and a vector field.

For a scalar field $f(\mathbf{r})$, the Laplacian is given by:

$$Lapl(f(\mathbf{r})) = \nabla^2 f(\mathbf{r}) = \nabla \bullet \nabla f(\mathbf{r}) \tag{A.8}$$

In Cartesian coordinates:

$$\nabla^2 f(\mathbf{r}) = \frac{\partial^2 f(\mathbf{r})}{\partial x^2} + \frac{\partial^2 f(\mathbf{r})}{\partial y^2} + \frac{\partial^2 f(\mathbf{r})}{\partial z^2} \tag{A.9}$$

Corresponding formulas for cylindrical and spherical coordinates can be found in [18].

For a vector field $\mathbf{V}(\mathbf{r})$, the Laplacian is defined by:

$$Lapl(\mathbf{V}(\mathbf{r})) = \nabla^2 \mathbf{V}(\mathbf{r}) = \nabla(\nabla \bullet \mathbf{V}(\mathbf{r})) - \nabla \times (\nabla \times \mathbf{V}(\mathbf{r})) \tag{A.10}$$

In Cartesian Coordinates:

$$\nabla^2 \mathbf{V}(\mathbf{r}) = (\nabla^2 V_x(\mathbf{r}))\hat{\mathbf{x}} + (\nabla^2 V_y(\mathbf{r}))\hat{\mathbf{y}} + (\nabla^2 V_x(\mathbf{r}))\hat{\mathbf{y}} \tag{A.11}$$

Thus the Laplacian of a vector field can be found by computing the Laplacian of its Cartesian components, which are scalar fields and thus one can use equation (A.9). The formulas for cylindrical and spherical coordinates are much more complex and can be found in [18]. The formula for cylindrical coordinates is given here as it is used in this thesis. If $\mathbf{V}(\mathbf{r}) = V_s(\mathbf{r})\hat{\mathbf{s}} + V_\phi(\mathbf{r})\hat{\phi} + V_z(\mathbf{r})\hat{\mathbf{z}}$, then:

$$\begin{aligned}
\nabla^2 \mathbf{V}(\mathbf{r}) = &\left(\frac{\partial^2 V_s(\mathbf{r})}{\partial s^2} + \frac{1}{s}\frac{\partial V_s(\mathbf{r})}{\partial s} - \frac{1}{s^2} V_s(\mathbf{r}) + \frac{1}{s^2}\frac{\partial^2 V_s(\mathbf{r})}{\partial \phi^2} - \frac{2}{s^2}\frac{\partial V_\phi(\mathbf{r})}{\partial \phi} + \frac{\partial^2 V_s(\mathbf{r})}{\partial z^2} \right) \hat{\mathbf{s}} \\
&+ \left(\frac{\partial^2 V_\phi(\mathbf{r})}{\partial s^2} + \frac{1}{s}\frac{\partial V_\phi(\mathbf{r})}{\partial s} - \frac{1}{s^2} V_\phi(\mathbf{r}) + \frac{1}{s^2}\frac{\partial^2 V_\phi(\mathbf{r})}{\partial \phi^2} + \frac{2}{s^2}\frac{\partial V_s(\mathbf{r})}{\partial \phi} + \frac{\partial^2 V_\phi(\mathbf{r})}{\partial z^2} \right) \hat{\phi} \\
&+ \left(\frac{\partial^2 V_z(\mathbf{r})}{\partial s^2} + \frac{1}{s}\frac{\partial V_z(\mathbf{r})}{\partial s} + \frac{1}{s^2}\frac{\partial^2 V_z(\mathbf{r})}{\partial \phi^2} + \frac{\partial^2 V_z(\mathbf{r})}{\partial z^2} \right)
\end{aligned} \tag{A.12}$$

Bibliography

[1] U. S. Naval Underwater Ordnance Station, "Electromagnetic radiation in sea water," April 1960.

[2] M. C. Domingo, "Magnetic Induction for Underwater Wireless Communication Networks," *IEEE Transactions on Antennas and Propagation*, vol. 60, pp. 2929–2939, June 2012.

[3] R. J. Urick, *Principles of Underwater Sound*, vol. 1. McGraw Hill, 1975.

[4] F. Tonolini and F. Adib, "Networking across boundaries: Enabling wireless communication through the water-air interface," 2018.

[5] R. Matheson, "Wireless communication breaks though water-air barrier," August 2018.

[6] D. Gibson, *Channel Characterisation and System Design for Sub-Surface Communications*. Leeds, Great Britain: Lulu Enterprises, 2010.

[7] J. R. Wait, "The Magnetic Dipole over the Horizontally Stratified Earth," vol. 29, pp. 577–592, 1951.

[8] S. H. Durrani, "Air to undersea communication with magnetic dipoles," 1964.

[9] P. N. W. J. J. Sojdehei and D. F. Dinn, "Magnetoinductive (mi) communications," vol. 1, pp. 513–519, 2001.

[10] K. Finkenzeller, *RFID Handbook*. Chichester UK: Wiley, 2001.

[11] L. Erdogan and J.-F. Bousquet, "Dynamic bandwidth extension of coil for underwater magneto-inductive communication," 2014.

[12] H. Guo, Z. Sun, and P. Wang, "Multiple Frequency Band Channel Modeling and Analysis for Magnetic Induction Communication in Practical Underwater Environments," *IEEE Transactions on Vehicular Technology*, vol. 66, pp. 6619–6632, August 2017.

[13] W. C. Chew, *Waves and Fields in Inhomogeneous Media*. IEEE PRESS Series on Electromagnetic Waves, 1995.

[14] M. C. Watson, J.-F. Bousquet, and A. Forget, "Evaluating the feasibility of magnetic induction to cross the air-water boundary," in *2021 Fifth Underwater Communications and Networking Conference (UComms)*, pp. 1–4, 2021.

[15] J. Y. P. P. C. J. S. Son Chu, Mark S. Luloff and E. Shamonina, "Magnetoinductive waves in attenuating media," 2021.

[16] Z. Tian, X. Zhang, and H. Wei, "A test of cross-border magnetic induction communication from water to air," 2022.

[17] J. D. Jackson, *Classical Electrodynamics Third Edition*. John Wiley and Sons Ltd, 1999.

[18] C. A. Balanis, *Antenna Theory: Analysis and Design*. Hoboken, New Jersey: Wiley, 2016.

[19] R. S. Elliott, *Electromagnetics*. IEEE Press, 1993.

[20] L. T. Corporation, "Lt1167 data sheet."

[21] F. S. Slobodan Babic and C. Akyel, "Validity check of mutual inductance formulas for circular filaments with lateral and angular misalignments," January 2009.